

1 Estimation of raindrop size distribution and rain rate with infrared 2 surveillance camera in dark conditions

3 Jinwook Lee¹, Jongyun Byun¹, Jongjin Baik¹, Changhyun Jun¹, Hyeon-Joon Kim¹

4 ¹Department of Civil and Environmental Engineering, College of Engineering, Chung-Ang University, Seoul, 06974, South
5 Korea

6 *Correspondence to:* Hyeon-Joon Kim (hjkim22@cau.ac.kr)

7 **Abstract.** This study estimated raindrop size distribution (DSD) and rainfall intensity with an infrared surveillance camera in
8 dark conditions. Accordingly, rain streaks were extracted using a k -nearest neighbor (KNN)-based algorithm. The rainfall
9 intensity was estimated using DSD based on physical optics analysis. The estimated DSD was verified using a disdrometer for
10 the two rainfall events. The results are summarized as follows. First, a KNN-based algorithm can accurately recognize rain
11 streaks from complex backgrounds captured by the camera. Second, the number concentration of raindrops obtained through
12 closed-circuit television (CCTV) images had values between $100 \text{ mm}^{-1}\text{m}^{-3}$ and $1,000 \text{ mm}^{-1}\text{m}^{-3}$, the root mean square error
13 (RMSE) for the number concentration by CCTV and PARTicle SIZE and VELOCITY (PARSIVEL) was $72.3 \text{ mm}^{-1}\text{m}^{-3}$ and 131.6
14 $\text{mm}^{-1}\text{m}^{-3}$ in the 0.5 to 1.5 mm section. Third, the maximum raindrop diameter and the number concentration of 1 mm or less
15 produced similar results during the period with a high ratio of diameters of 3 mm or less. Finally, after comparing with the 15-
16 min cumulative PARSIVEL rain rate, the mean absolute percent error (MAPE) was 49% and 23%, respectively. In addition,
17 the differences according to rain rate can be found that the MAPE was 36% at a rain rate of less than 2 mm h^{-1} and 80% at a
18 rate above 2 mm h^{-1} . Also, when the rain rate was greater than 5 mm h^{-1} , MAPE was 33%. We confirmed the possibility of
19 estimating an image-based DSD and rain rate obtained based on low-cost equipment during dark conditions.

20 1 Introduction

21 Precipitation data is vital in water resource management, hydrological research, and global change analysis. The primary means
22 of measuring precipitation is to use a rain gauge (Allamano et al., 2015) to collect raindrops from the ground. Due to the
23 restrictions on the installation environment of the rain gauge, it can be difficult to understand the spatial rainfall distribution
24 in mountains and urban areas (Kidd et al., 2017). Furthermore, the tipping-bucket-type rain gauge, which accounts for most
25 rain gauges, has a discrete observation resolution (0.1 or 0.5 mm) for the discrete time steps, producing uncertainty in temporal
26 rainfall variation. For this reason, weighing gauges are nowadays used very often instead of tipping-bucket-type. the weighing
27 gauge is a meteorological instrument used to observe and analyze various precipitation, including rainfall and snowfall. Also,
28 the tipping bucket has a large error due to the observation time delay when the rainfall is less than 10 mm h^{-1} compared to the

29 weighing gauge. However, when the observation time size is set to 10 to 15 minutes, the relative percentage error has a very
30 low value of -6.7 to 2.5%, resulting in high accuracy (Colli et al., 2014).

31 In contrast, it is possible to obtain spatial rainfall information on a global scale with remote sensing techniques (Famiglietti
32 et al., 2015). However, remote sensing techniques provide only indirect measurements that must be continuously calibrated
33 and verified through ground-level precipitation measurements (Michaelides et al., 2009). Recently, a disdrometer capable of
34 investigating the microphysics characteristics of rainfall has been used for observation instead of the traditional rainfall
35 observation instrument (Kathiravelu et al., 2016). However, these devices cannot be widely installed because of their high cost
36 and difficulty in accessing observational data. Consequently, a high-resolution and low-cost ground precipitation monitoring
37 network has not yet been established.

38 With the advent of the Internet of Things (IoT) era, using non-traditional sources is attractive for improving the
39 spatiotemporal scale of existing observation networks (McCabe et al., 2017). In recent years, such cases have been common
40 in rainfall observation. For example, there have been attempts to estimate rainfall using sensors to capture signal attenuation
41 characteristics in commercial cellular communication networks (Overeem et al., 2016), vehicle wipers (Raibei et al., 2013),
42 and smartphones (Guo et al., 2019). Furthermore, crowdsourcing information has been used to confirm the utility of estimating
43 regional rainfall (Haberlandt and Sester, 2010; Rabiei et al., 2016; Yang and Ng, 2017).

44 In a similar context, a surveillance camera is a sensor with high potential. Surveillance cameras are often referred to as
45 closed-circuit television (CCTV). Compared with other crowdsourcing methods, the visualization data of surveillance cameras
46 are highly intuitive (Guo et al., 2017). Therefore, they have been used in various fields (Cai et al., 2017; Nottle et al., 2017;
47 Hua, 2018). In Korea, public surveillance camera installations have been rapidly increasing, from approximately 150,000 in
48 2008 to 1.34 million in 2020—approximately a public CCTV camera per 0.07 km². Thus, the potential for precipitation
49 estimation using camera sensing is expected to be greater in Korea.

50 Recently, various studies have been conducted to estimate rainfall intensity using the rain streak image obtained from
51 surveillance camera videos. Many studies attempted to use artificial intelligence to capture changes in the image captured by
52 the camera when it rains (Zen et al., 2019; Avanzato and Beritelli, 2020; Wang et al., 2022). In contrast, some studies have
53 tried to estimate rainfall intensity using geometrical optics and photographic analyses. Typically, the rain streak layer is
54 separated from the raw image or video. A rain streak is the visual appearance of raindrops caused by visual persistence—
55 raindrops falling because of the blur phenomenon of raindrop movement from the camera's exposure time appears as streaks
56 on the image. Garg and Nayar (2005) made one of the first attempts to measure this rainfall.

57 These previous studies indeed confirmed the possibility of rainfall measurement using surveillance cameras. However,
58 several limitations still prevent the actual expansion of the measurement systems using surveillance cameras. In general, most
59 surveillance cameras are installed for monitoring purposes, and people's faces are inevitably captured. Therefore, it is not easy
60 to disclose the data due to privacy concerns. Data storage and transmission are also limitations. Since most surveillance
61 cameras use a hard disk, data must be taken out directly. In other words, rainfall estimation cannot be done in real-time unless
62 a system is in place to transmit data over the Internet. In addition, the applicability to night-time is more limited. In the case of

63 general surveillance cameras in the past, observation is possible only when sunlight exists. For the observation system to
64 expand, these various limitations must be addressed, and it seems that a lot of time and effort are needed. Nevertheless, research
65 to develop algorithms using surveillance cameras in various conditions and to confirm applicability can have sufficient
66 meaning. The case of dark conditions is one of the conditions worth studying. This is because the recently installed surveillance
67 cameras are equipped with an infrared recording function, so most cameras will be able to take videos at night soon. However,
68 the final purpose of utilizing these devices and the method is not to replace existing devices. It could be a supplement to
69 improve the spatiotemporal resolution and accuracy of existing observation instruments. In particular, a study on the drop size
70 distribution of rainfall, rather than simple rainfall estimation, would have more potential application value.

71 Since then, many studies have been conducted to develop and improve efficient algorithms. Allamano et al. (2015)
72 proposed a framework to estimate the quantitative rainfall intensity using camera images based on physical optics from a
73 hydrological perspective. Dong et al. (2017) proposed a more robust approach to identifying raindrops and estimating rainfall
74 using a grayscale function, making grayscale subtraction nonlinear. Jiang et al. (2019) proposed an algorithm that decomposes
75 rain-containing images into rain streak layers and rainless background layers using convex optimization algorithms and
76 estimates instantaneous rainfall intensity through geometric optical analysis.

77 Some studies (e.g., Dong et al., 2017) have sought to estimate raindrop size distribution (DSD) using a surveillance camera.
78 However, the existing studies have focused on the time when video can be captured with visible light. It is impossible to obtain
79 input data without visible light using the existing image-based rainfall measurement method. Thus, these methodologies are
80 only applicable in daytime conditions. However, when recording using infrared rays, it is possible to obtain a rainfall image
81 even when there is no sunlight. No study has estimated the rain in dark conditions to our knowledge. Furthermore, most
82 previous studies did not verify the estimated DSD using a disdrometer. In contrast, this study estimated DSD with an infrared
83 surveillance camera in dark conditions, based on which rainfall intensity was also estimated. Rain streaks were extracted using
84 a k-nearest neighbor (KNN)-based algorithm. The DSD was used to calculate rainfall intensity with physical optics analysis
85 and verified using a PARticle SIze and VELOCITY (PARSIVEL) disdrometer (Löffler-Mang and Joss, 2000).

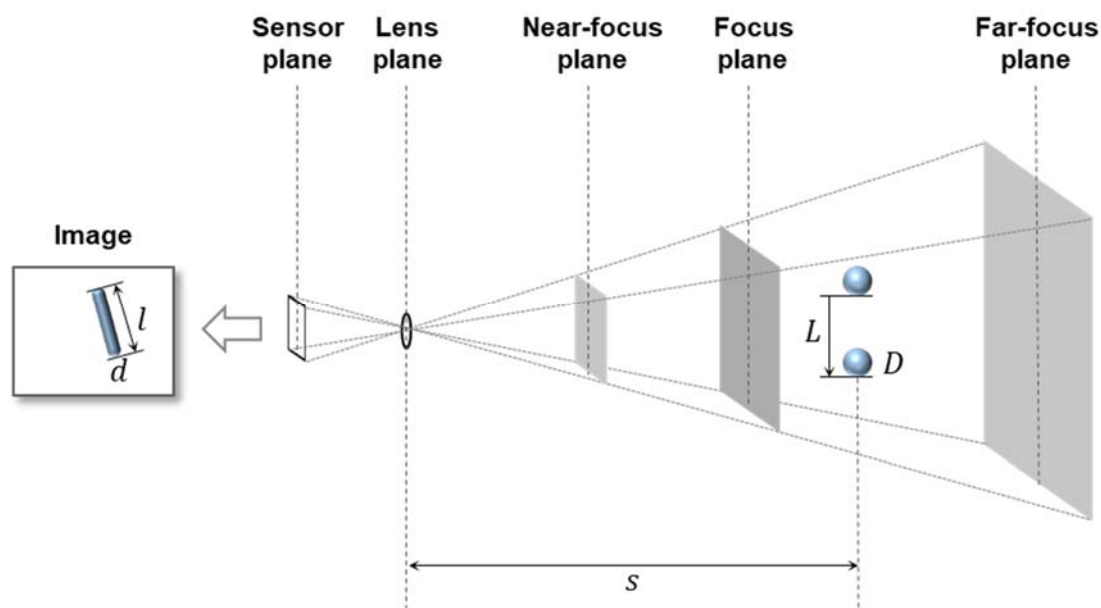
86 **2 Methodology**

87 **2.1 Recording video containing rain streaks using an infrared surveillance camera**

88 The surveillance camera records video. The video looks continuous, but it is also composed of discrete still images, so-called
89 frames. The frequency of recording frames (i.e., acquisition rate) is called frame per second (fps). In other words, fps is how
90 many images are taken per second for recording video. Another important factor in video recording is exposure time. Exposure
91 time, also called shutter speed, refers to the time the camera sensor is exposed to light to capture a single frame. The real
92 raindrops are close to a circle, but in a single image, the raindrops look like a streak. This is because raindrops move at a high
93 speed during the exposure time. Therefore, the raindrops that moved during the exposure time are visualized in the rain streaks
94 in a single frame.

95 Fig. 1 shows an example of capturing a raindrop for a single frame. Here, only the raindrops near the point of focus are
 96 visible, and objects that are more than a certain distance appear invisible. That is, the point where the focus is best is called the
 97 focus plane, and there is a range in which it can be recognized that objects are focused before and after the focus plane. The
 98 closest plane that can be considered to be in focus is called the near-focus plane, and the farthest plane is called the far-focus
 99 plane. This range is generally called depth of field (DoF). Ultimately, the rainfall intensity can be estimated based on the
 100 volume and raindrops in the DoF.

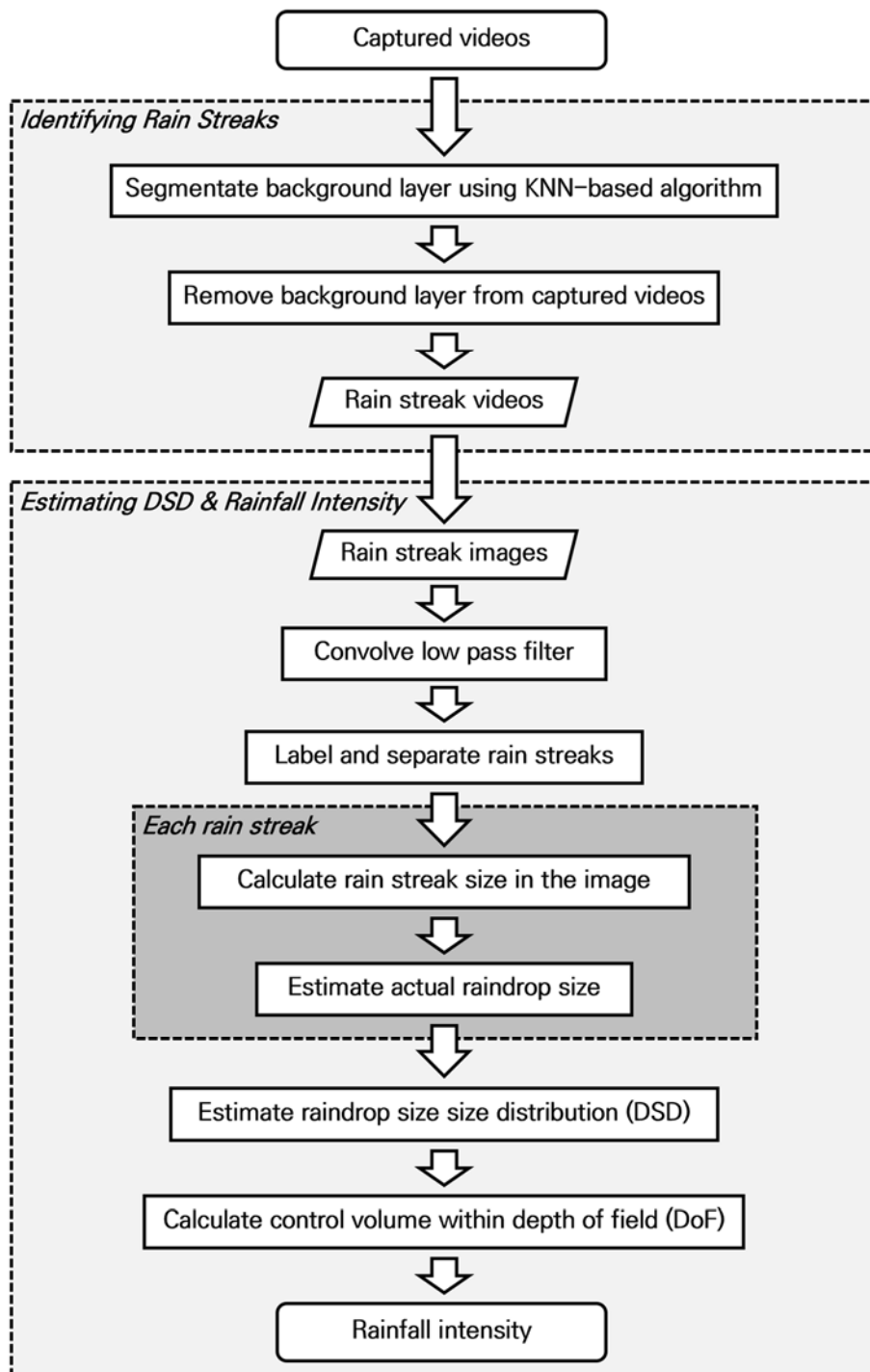
101 In this study, an infrared surveillance camera was considered under dark conditions. Here, the dark condition refers to a
 102 condition in which raindrops cannot be captured by a general surveillance camera with visible light. Infrared cameras emit
 103 near-infrared rays through an infrared emitter and receive the reflected light from the objects. Accordingly, it has the advantage
 104 of being able to detect raindrops that are invisible to the human eye.



105 **Figure 1. Schematic diagram of the photographed rain streak in the image and the movement of a raindrop during the exposure**
 106 **time.**

107 2.2 Algorithm for identifying rain steaks and estimating DSD and rain rate

108 Image-based rainfall estimation can be divided into two processes: identifying rainfall streaks and estimating DSD. Fig. 2
 109 illustrates these processes in a flowchart. Identifying rain streaks requires an algorithm that separates the moving rain streaks
 110 from the background layer. Next, in estimating DSD, raindrops are extracted from the image of the rain streaks, and the overall
 111 distribution is obtained.



112 Figure 2. Flowchart of the methodology for estimating DSD and rainfall intensity.

113 Most existing algorithms aim to remove raindrops in images because raindrops are considered noise in object detection
114 and tracking (Duthon et al., 2018). Such algorithms are categorized into multiple-image-based and single-image-based
115 approaches (Jiang et al., 2018).

116 For example, Garg and Nayar (2007) classified the conditions in which the brightness difference between the previous
117 pixel and that of the next pixel exceeds a specific threshold over time, assuming that the background is fixed. Improved
118 algorithms were then developed considering the temporal correlation of raindrops (Kim et al., 2015) and chromatic properties
119 (Santhaseelan and Asari, 2015). Tripathi and Mukhopadhyay (2014) proposed a framework that removes rain that reduces the
120 visibility of the scene to improve the detection performance of image feature information. However, single-image-based
121 algorithms rely more on the properties of raindrops (Deng et al., 2018). The central idea of a single-image-based algorithm is
122 to decompose rain-containing images into rainless layers (Li et al., 2016; Deng et al., 2018; Jiang et al., 2018).

123 An image including grayscale rainfall may be mathematically expressed in a two-dimensional (2D) matrix in which each
124 element has a grayscale value. A single image ($m \times n$) is expressed as follows (Jiang et al., 2018):

$$125 \quad O = B + R, \tag{1}$$

126 where $O \in R^{m \times n}$, $B \in R^{m \times n}$, and $R \in R^{m \times n}$ are the raw image, rain-free background layer, and rain streak layer.

127 Accordingly, various algorithms are available for rain streak identification. Different still image and video-based
128 algorithms have been proposed to eliminate objects such as moving objects for application to actual surveillance cameras.
129 However, most of these algorithms face optimization problems because of the vast number of decision variables (Jiang et al.,
130 2019). This task is not easy to solve or requires excessive computation time. Therefore, existing studies present techniques
131 suitable for post-analysis rather than application in real-time. The use of complex algorithms can increase versatility and
132 accuracy, but there is a trade-off that reduces computational speed. The time required for such computing is a critical
133 disadvantage in practical applications for estimating rainfall intensity.

134 In this study, a KNN-based segmentation algorithm (Zivkovic and Heijden, 2006), a popular non-parametrical method for
135 background subtraction, was considered for segmenting the rain streaks (foreground) and background layers. KNN is used in
136 classification and regression problems (Bouwman et al., 2010). The concept of KNN is that similar things are close—the
137 KNN-based segmentation algorithm finds the closest k samples (neighbors) to the unknown sample using Euclidean distance
138 to determine the class (i.e., foreground or background). Thus, the KNN-based segmentation method to detect foreground
139 changes in the video was used to identify rain streaks by recording infrared videos under conditions with little background
140 influence. In the algorithm, The KNN subtractor works by updating the parameters of a Gaussian mixture model for more
141 accurate kernel density estimation (Trnovszký et al., 2017). KNN is more efficient for local density estimation (Qasim et al.,
142 2021); therefore, the algorithm is highly efficient if the number of foreground pixels is low.

143 We used the package provided by OpenCV to implement the KNN-based segmentation algorithm (Zivkovic and Heijden,
144 2006). Accordingly, three main parameters (history, dist2Threshold, detectShadows) needed to be set. Table 1 presents the
145 description of the parameters used for the KNN background subtractor package.

146 **Table 1. Parameters in KNN background subtractor package in OpenCV.**

Parameter	Description
history	Length of the history
dist2Threshold	Threshold on the squared distance between the pixel and the sample to decide whether a pixel is close to that sample. This parameter does not affect the background update.
detectShadows	If true, the algorithm will detect shadows and mark them. This decreases the speed slightly, so if you do not need this feature, set the parameter to false.

147 It is essential to capture raindrops within the camera's depth of field (DoF) to calculate the final DSD and rainfall intensity.
 148 Accordingly, this study proposed a novel algorithm to extract each rain streak from the rain streaks image. First, we applied a
 149 low-pass filter to the rain streaks image to remove unfocused raindrops that may remain in the image, which smooths each
 150 pixel using a 2D kernel. Videos from infrared mode have usually a blur effect. Thus, the additional 2D kernel was applied to
 151 remove the pixels having blur. Highly detailed parts (e.g., out-of-focus raindrops and some noises) are erased, leaving some
 152 clear rain streaks. A background layer with a value of 0 and a part not in the image were separated to extract the rain streaks
 153 and labeled one by one to identify each rain streak from the image.

154 Because the rain streak observed in the surveillance camera image causes an angle difference (influenced by the wind), a
 155 diameter estimation process considering the angle of the rain streak (fall angle of a raindrop) is required. If the angle of rain
 156 steak is considered and converted to the raindrop diameter through the horizontal pixel size in the image, the shape change in
 157 the raindrop because of air buoyancy (i.e., during the falling of the raindrop) may not be reflected, and overestimation can
 158 occur.

159 Accordingly, the representative angle of each extracted rain streak was calculated. The border information of each rain
 160 streak was obtained, and the center axis information of the rain streak was obtained based on the border information to calculate
 161 the drop angle. Moreover, the rain streak was rotated to set the long and short axes of the streak at 0° and 90°, using the angle
 162 information.

163 The size of raindrops in the rain streaks image can be estimated through the analysis of microphysical characteristics of the
 164 raindrop and geometric optical analysis (Keating, 2002). The instantaneous velocity of a raindrop on the ground can be
 165 estimated from the exposure time and the size of the raindrop. However, the distance from the raindrop to the lens surface (i.e.,
 166 the object distance) is unknown and should be inferred. Object distance can be calculated through physical optics analysis
 167 because it causes perspective distortion. Assuming a raindrop is spherical, the length of the trajectory where the raindrop falls
 168 when the camera is exposed and the diameter of the raindrop can be inferred through the lens equation (Keating, 2002):

$$169 \quad L(s) = \frac{d_f - f}{d_f \cdot f} \frac{h_s}{h_p} l_p s, \quad (2)$$

$$170 \quad D(s) = \frac{d_f - f}{d_f \cdot f} \frac{w_s}{w_p} d_p s, \quad (3)$$

171 where s is the distance from the raindrop to the lens plane (mm). $L(s)$ and $D(s)$ are the length of falling trajectory during camera
 172 exposure (rain streak) and the raindrop's diameter. d_f is the focus distance (mm), and f is the focal length (mm). h_s and w_s are
 173 the vertical and horizontal sizes of the active area of the image sensor (mm), and h_p and w_p are the vertical and horizontal sizes
 174 of the captured image (in the number of pixels). l_p and d_p are the length and width of the rain streaks in the image (in the
 175 number of pixels).

176 It is then possible to infer the falling speed of raindrops using the camera's exposure time (Jiang et al., 2019), as follows:

$$177 \quad v(s) = \frac{L(s)}{1000\tau}, \quad (4)$$

178 where τ is the exposure time of the camera (seconds) and $v(s)$ is the fall velocity of the raindrop from the image. Furthermore,
 179 the fall velocity of a raindrop can be approximated by an empirical formula for raindrop diameter. The most frequently used
 180 equation is as follows (Atlas et al., 1973; Friedrich et al., 2013):

$$181 \quad v(D) = 9.65 - 10.3\exp(-0.6D), \quad (5)$$

182 where D is the raindrop diameter and v is the fall velocity of the raindrop. The actual diameter of raindrops can be obtained by
 183 solving the equation with the fall velocity obtained through the exposure time and Eqs. (4) and (5). Furthermore, the DoF for
 184 the images using the camera's setting information can be calculated, and the effective volume for estimating rainfall intensity
 185 can be obtained. Details of the process are described in previous studies (Allamano et al., 2015; Jiang et al., 2019).

186 The control volume must be determined to estimate the rainfall intensity using the diameter of each raindrop. An understanding
 187 of DoF is required to achieve the volume. The DoF is simply the range at which the camera can accurately focus and capture
 188 the raindrops. Calculating this range requires obtaining the near and far focus planes as follows:

$$189 \quad s_n = \frac{d_f \cdot f^2}{f^2 + N \cdot c_p \cdot (d_f - f)}, \quad (6)$$

$$190 \quad s_f = \frac{d_f \cdot f^2}{f^2 - N \cdot c_p \cdot (d_f - f)}, \quad (7)$$

191 where s_n and s_f are the distances from the near and far focus planes. c_p is the maximum permissible circle of confusion, a
 192 constant determined by the camera manufacturers. N is the F-number of the lens relevant to the aperture diameter. Accordingly,
 193 the theoretical sampling volume (V , m^3) indicates the truncated rectangular pyramid between the near and far focus planes:

$$194 \quad V = \frac{1}{3 \cdot 10^9} \left(\frac{d_f - f}{d_f \cdot f} \right)^2 w_s h_s (s_f^3 - s_n^3), \quad (8)$$

195

196 Then, we used the gamma distribution equation, Eq. (6), proposed by Ulbrich (1983), to calculate DSD parameters using
 197 data at every 1 min interval.

$$198 \quad N(D) = N_0 D^\mu \exp(-\lambda D), \quad (9)$$

199 where $N(D)$ ($\text{mm}^{-1}\text{m}^{-3}$) is the number concentration value per unit volume for each size channel, and N_0 ($\text{mm}^{-1-\mu}\text{m}^{-3}$) is an
 200 intercept parameter representing the number concentration when the diameter has 0 value. D (mm) and Λ (mm^{-1}) are the drop
 201 diameter and slope parameter. Raindrops smaller than 8.0 mm were used to avoid considering non-weather data such as leaps
 202 and bugs (Friedrich et al., 2013).

203 The gamma distribution relationship is a function of formulating the number concentration per unit diameter and unit
 204 volume. It was proposed by Marshall and Palmer (1948) as an improved model of exponential distribution as a favorable form
 205 to reflect various rainfall characteristics. By including the term containing μ in the distribution function, the shape of the
 206 number concentration distribution for small drops smaller than 1 mm is improved.

$$207 \quad N(D) = N_0 \exp(-\Lambda D), \quad (10)$$

208 As the Λ decreases, the slope of the distribution shape decreases, and the proportion of the large drops increases. Conversely,
 209 as the value increases, the distribution slope becomes steeper, and the weight of the large particles decreases. When μ has a
 210 large value, the distribution is convex upward, and it has a distribution with a sharp decrease in number concentration at small
 211 diameters. Whereas when it has a negative value, the distribution is convex downward with an increase in the concentration
 212 of drops smaller than 1 mm. In the gamma distribution, the μ is mainly affected by the difference in concentration of raindrops
 213 smaller than 3 mm (Vivekanandan et al., 2004).

214 Vivekanandan et al. (2004) explained the reason for using the gamma distribution as follows. First, it is sufficient to
 215 calculate the rainfall estimation equation using only the first, third, and fourth moments (Eq. (11)) (Smith, 2003). Second, the
 216 long-term raindrop size distribution has an exponential distribution shape (Yuter and Houze, 1997).

217 The raindrop size distribution observed from the ground is the result of the microphysical development of raindrops falling
 218 from precipitation clouds. The drop size distribution shape is changed during fall by microphysical processes such as collision,
 219 merging, and evaporation, and changes in the concentration of drops larger than 7.5 mm and small drops occur mainly. As a
 220 result, the drop size distribution observed on the ground mainly follows the gamma distribution shape (Ulbrich, 1983; Tokay
 221 and Short, 1996). The gamma distribution relationship should be used to analyze the distribution of raindrops that are actually
 222 floating and falling.

$$223 \quad M_n = \int_{D_{min}}^{D_{max}} D^n N(D) dD, \quad (11)$$

224 Eq. (11) indicates a moment expression for the n^{th} order. For example, the second moment is calculated as the product of
 225 the square of the diameter of each channel and the number concentration and the diameter of each channel. Each moment value
 226 has a different microphysical meaning. Therefore, the gamma distribution including three dependent parameters is more
 227 advantageous in reflecting the microphysical characteristics of the precipitation system than the exponential distribution
 228 including two dependent parameters. Eq. (11) can be expressed in gamma distribution format as follows:

$$229 \quad M_n = \int_{D_{min}}^{D_{max}} D^n N(D) dD = N_0 \Lambda^{-(\mu+n+1)} \Gamma(\mu + n + 1), \quad (12)$$

230 where N_T (total number concentration, m^{-3}) is the zero-order moment (M_0) and represents the total number concentration of
 231 raindrops per unit volume. η was determined for calculating μ and Λ . In this study, a combination of moments in the ratio of
 232 M_2 , M_4 , and M_6 , which accurately represents the characteristics of small raindrops, was applied (Vivekanandan et al., 2004):

$$233 \quad \eta = \frac{\langle M_4 \rangle^2}{\langle M_2 \rangle \langle M_6 \rangle} = \frac{(\mu+3)(\mu+4)}{(\mu+5)(\mu+6)}, \quad (13)$$

234 μ and Λ are calculated as follows:

$$235 \quad \mu = \frac{(7-11\eta) - [(7-11\eta)^2 - 4(\eta-1)(30\eta-12)]^{1/2}}{2(\eta-1)}, \quad (14)$$

$$236 \quad \Lambda = \left[\frac{M_2 \Gamma(\mu+5)}{M_4 \Gamma(\mu+3)} \right]^{1/2} = \left[\frac{M_2(\mu+4)(\mu+3)}{M_4} \right]^{1/2}, \quad (15)$$

237 A larger value of D_m (mm) estimated using Eq. (16), the diameter of the average mass of raindrops contained in the unit
 238 volume, indicates that predominantly larger drops are distributed.

$$239 \quad D_m = \frac{M_4}{M_3}, \quad (16)$$

240 R ($mm\ h^{-1}$) is the rain rate calculated using Eq. (17).

$$241 \quad R = \frac{6\pi}{10^4} \int_{D_{min}}^{D_{max}} D^3 N(D) V(D) dD, \quad (17)$$

242 3 Study site and observation equipment

243 This study used a building's rooftop as the study site. The building is the Chung-Ang University's Bobst Hall, located in the
 244 central region of Seoul in Korea. It is located at $37^\circ 30' 13''$ north latitude and $126^\circ 57' 27''$ east longitude, at an elevation of
 245 42 m. Fig. 3 illustrates the CCTV (marked with a red circle) and PARSIVEL installed at the study site. The CCTV was used
 246 for the main analysis, and PARSIVEL was considered for verification purposes.



(a) Surveillance camera



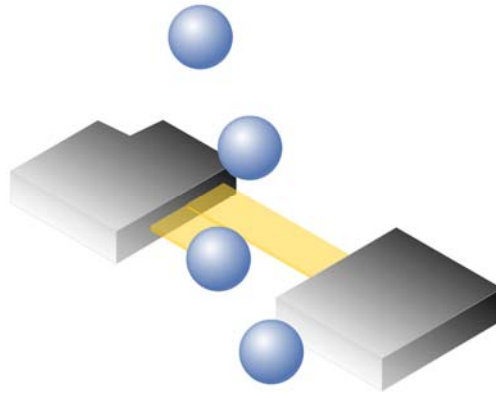
(b) PARSIVEL

247 **Figure 3. Observation measurements considered in this study.**

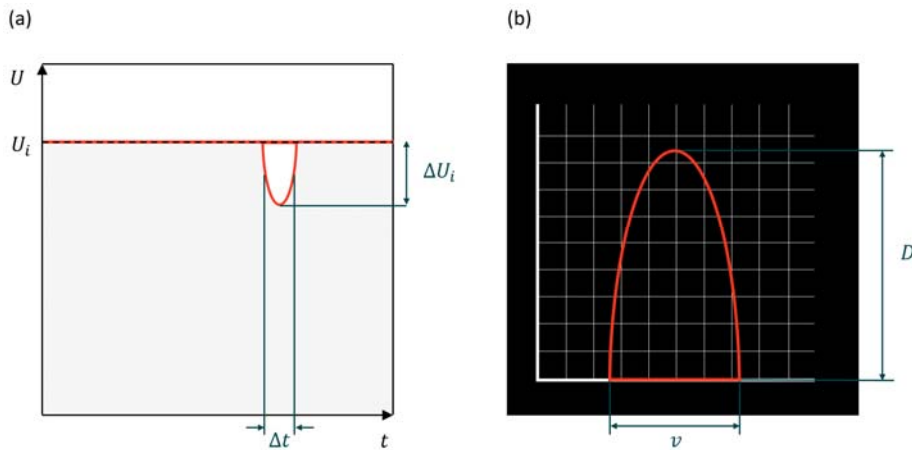
248 The CCTV model used in this study is DC-T333CHRX, developed by IDIS. The camera has a 1/1.7 inch complementary
249 metal-oxide semiconductor (CMOS) with a height and width of 5.70 mm and 7.60 mm. The focal length is 4.5 mm, and the
250 F-number of the lens is 1.6. The shutter speed was set to 1/250 s, and the frame per second (fps) was set to 30. The infrared
251 ray distance is 50 m. The maximum permissible circle of confusion is 0.005 mm. The camera's resolution is 1,080 pixels for
252 the height and 1,920 pixels for the width, but the cropped images (640×640 pixels) were considered for the analysis.

253 The PARSIVEL is a ground meteorological instrument that can observe precipitation particles' diameter and fall speed
254 (e.g., raindrops, snow particles, hail). The meteorological information, including raindrop size, is used to estimate the
255 quantitative precipitation amount and reveal the precipitation system's microphysical characteristics and development
256 mechanism.

257 The PARSIVEL used in this study is the second version of the instrument manufactured by OTT in Germany, and it is
258 improved the observation accuracy of small particles. The PARSIVEL uses a laser-based optical sensor to send a laser from
259 the transmitter and continuously receive it from the receiver (Fig. 4). As the laser beam moves from the transmitter to the
260 receiver, the precipitation particle passes over the laser beam, and the size and velocity of the precipitation particle are observed
261 (Nemeth and Hahn, 2005). The diameter and velocity of the particle are calculated by calculating the time the particle passes
262 through the laser and the laser intensity that decreases during the passage (Fig. 5).



263 **Figure 4. Functional principle of the PARSIVEL disdrometer.**



264 **Figure 5. (a) Signal changes whenever a particle falls through the beam anywhere within the measurement area. (b) The degree of**
 265 **dimming is a measure of the particle's size; together with the duration of the signal, the fall velocity can be derived.**

266 Parameters such as rain rate, reflectivity, and momentum of raindrops are calculated through particle concentration values
 267 for each diameter and falling speed channel obtained through PARSIVEL observation. In this study, the temporal resolution
 268 of the observation data was set to 1 minute. The particle diameters from 0.2 to 25 mm (Table 1 in Appendix) and fall velocity
 269 from 0.2 to 20 m s⁻¹ (Table 2 in Appendix) can be observed by the PARSIVEL. The particle diameter and the fall speed each
 270 have 32 observation channels, so the number of observed particles for the time resolution set in 1,024 channels (32×32) is
 271 observed. The first and second channels of diameter are not included in the observable range of the PARSIVEL and are treated
 272 as noise. Therefore, the observation data of the first and second diameter channels were not considered in the actual analysis.
 273 The detailed information on the specifications of the PARSIVEL is presented in Table 2.

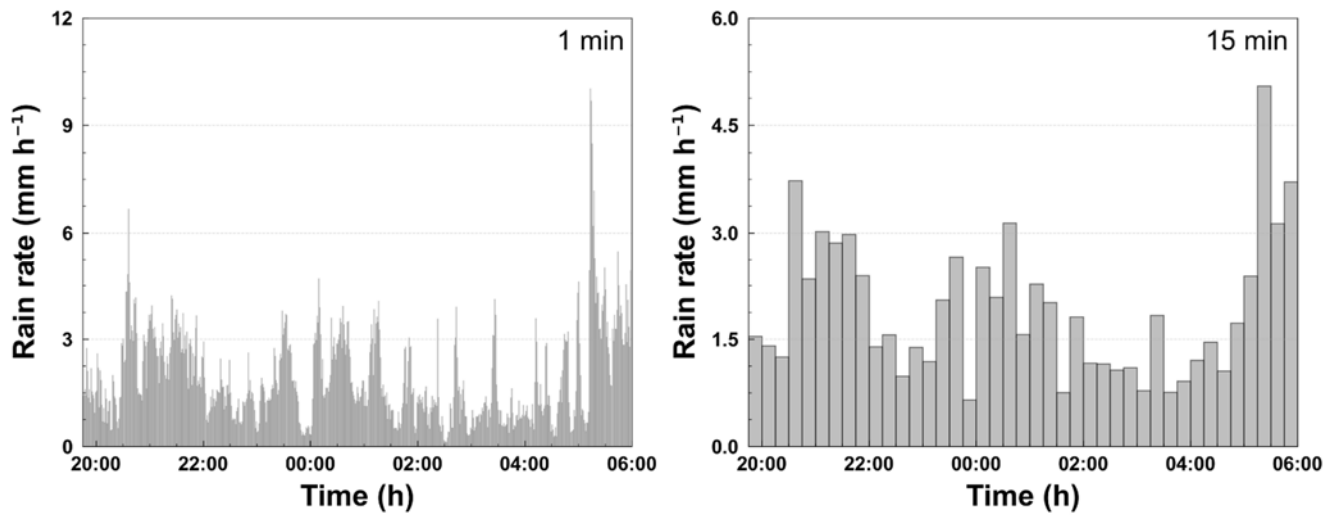
274 **Table 2. Technical information of the PARSIVEL disdrometer.**

Wavelength of optical sensor		780 nm
Measuring area		30 × 180 mm (54 cm ²)
Measuring range	Size	0.2 ~ 25 mm (32 channel class)
	Fall velocity	0.2 ~ 20 m s ⁻¹ (32 channel class)
Precipitation intensity		0.001 ~ 1,200 mm h ⁻¹
Measurement time interval		10 sec ~ 60 min
Instrument dimensions (H×W×D)		670 × 600 × 114 mm

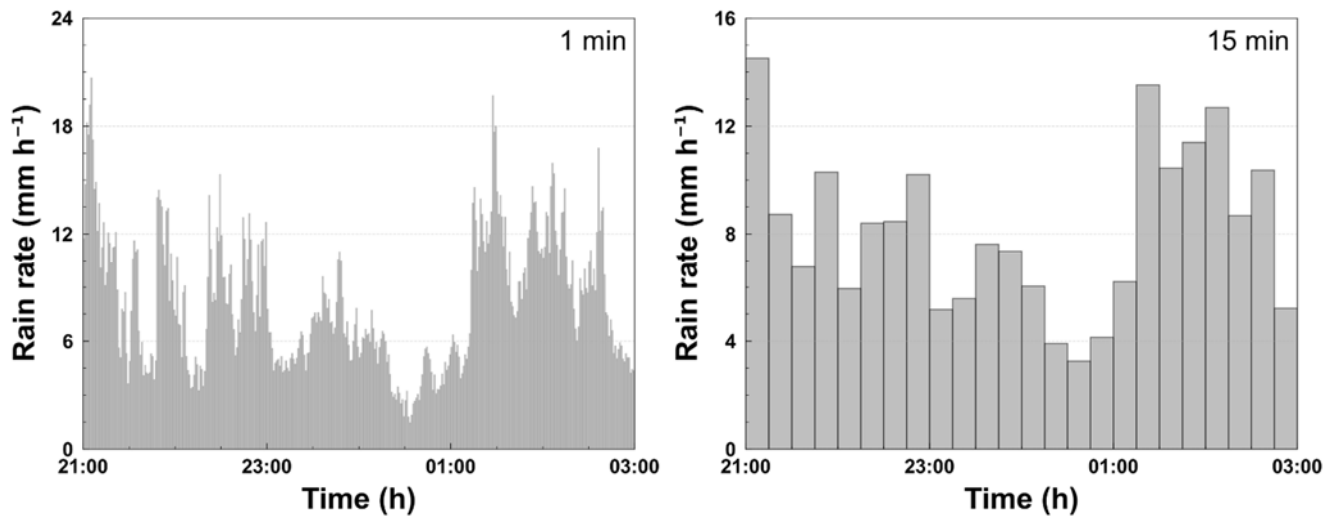
275 **4 Application result**

276 **4.1 Rainfall event**

277 We considered two rainfall events from 1945 LST on March 25, 2022, to 0615 LST on March 26, 2022 (case 1), and 2100
278 LST on September 5, 2022, to 0300 LST on September 6, 2022 (case 2). Fig. 6 illustrates the hyetographs of the rainfall event
279 considered in this study according to the time resolution. The total rainfall of case 1 and 2 is 19.5 and 48.7 mm based on the
280 PARSIVEL, respectively. The maximum rain rate is 10.0 and 20.7 mm h⁻¹ based on the 1 min resolution, and 5.0 and 14.5 mm
281 h⁻¹ based on the 15 min resolution for case 1 and case 2.



(a) Case 1



(b) Case 2

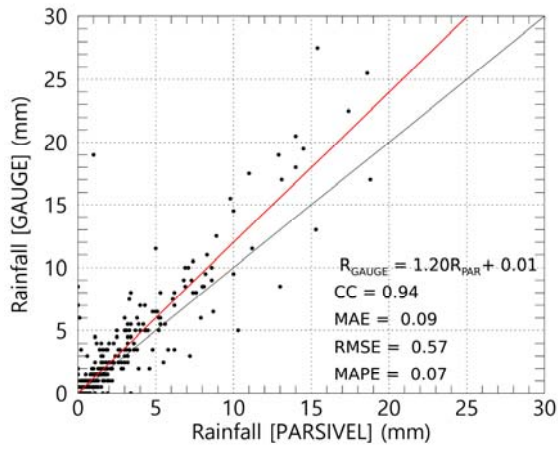
282 **Figure 6. Hyetograph of PARSIVEL and rain gauge observation data for the rainfall events considered in this study (left: 1 min**
 283 **resolution, right: 10 min resolution).**

284 In order to secure the quantitative reliability of the PARSIVEL observation data, rain gauge observation data were used to
 285 verify the rainfall calculated through the PARSIVEL observation. The rainfall data used for verification are rain gauge
 286 observation data operated by KMA (Korea Meteorological Administration) installed closer than 4 km from the PARSIVEL
 287 observation site (Table 3). The rainfall comparison period is from September 14, 2021, to October 4, 2022, including the period
 288 of the analysis case. Fig. 7 shows scatter plots comparing hourly rain rates from rain gauges and PARSIVEL. As a result of
 289 comparison with the observation data at three rain gauge sites, it had low MAE (Mean Absolute Error), RMSE (Root Mean
 290 Square Error), MAPE (Mean Absolute Percent Error) values of less than 0.11 mm h⁻¹, 0.6 mm h⁻¹, and 8%. Also, correlation
 291 values were more than 0.9.

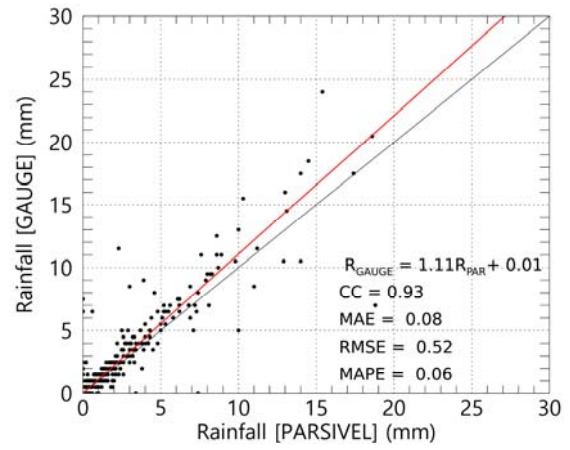
292 **Table 3. Location information of rain gauge observation sites.**

Rain gauge site	Latitude (°)	Longitude (°)	Range from PARSIVEL site (km)
G1	37.4933	126.9175	3.73
G2	37.5196	126.9763	2.42
G3	37.5249	126.9390	2.87

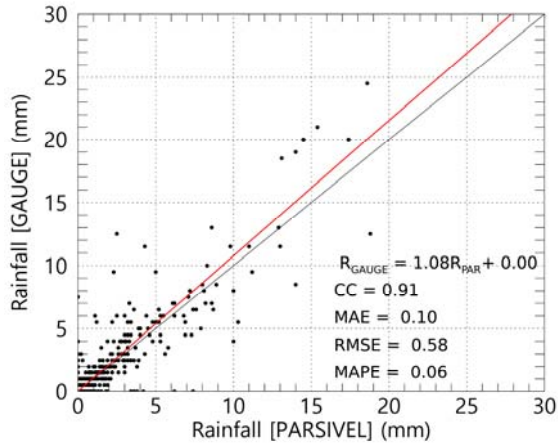
293



(a) G1



(b) G2

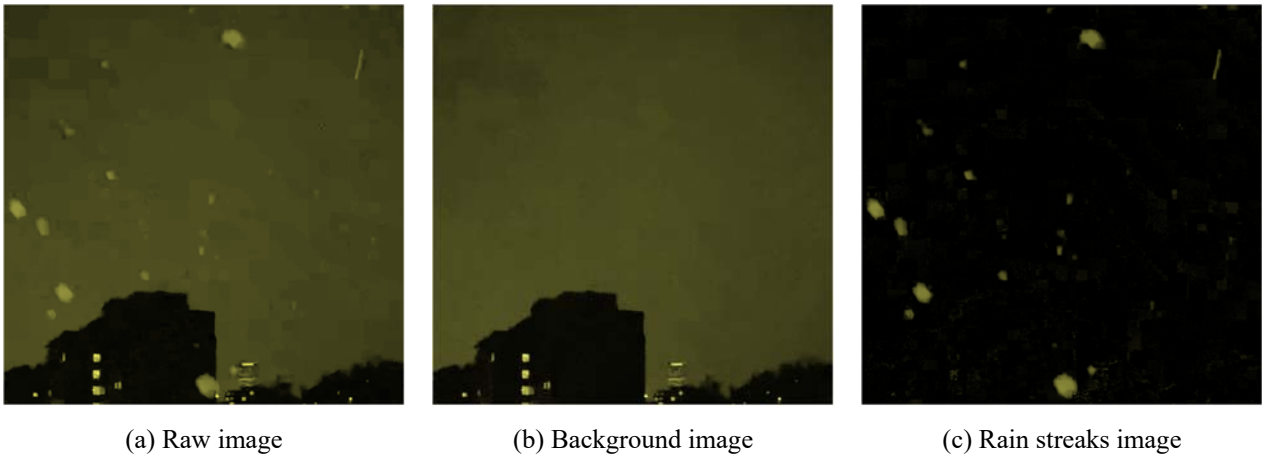


(a) G3

294 **Figure 7. Scatter plot of rainfall amount every 1 hour from the PARSIVEL observation and the rain gauge observation.**

295 **4.2 Identifying rainfall streaks**

296 The rain streaks were distinguished from the original raw images using the KNN-based algorithm described in Section 2.2.
 297 Accordingly, two parameters (history and dist2Threshold) were set to default values (500 and 400). The other parameter
 298 (detectShadows) was set to “false.” Fig. 8 illustrates the raw, background, and rain streaks images for an example time image
 299 (20:30:57 March 25, 2022), scaled in yellow to make it easier to verify the visual change.



300 **Figure 8. Segmentation example of a raw image into background and rain streaks image based on KNN-based algorithm (20:30:57**
 301 **March 25, 2022).**

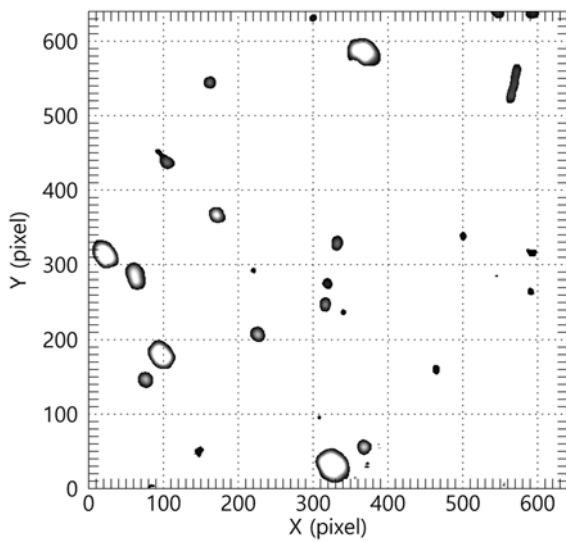
302 As confirmed in Fig. 8, adequate background separation performance can be achieved using the KNN-based method used
 303 in this study. Because it is an infrared camera and the camera's exposure time is 1/250 s, the length of rain streaks is relatively
 304 short. The longer the exposure time, the longer the raindrops appear on the image (Schmidt et al., 2012; Allamano et al., 2015).
 305 If the exposure time is too long, some rain streaks may penetrate the image. In this case, it is difficult to estimate the rain streak
 306 length, a clue for estimating raindrop size.

307 The identification algorithm was implemented using Anaconda Software Distribution on a workstation with an AMD Ryzen
 308 5 5600X 6-Core Processor and 32 GB RAM. The computing time for the 15 min video was approximately 50 s using only
 309 CPU computation. As described previously, the KNN-based algorithm used in this study has high-speed computing
 310 performance compared with various algorithms based on optimization, so it will likely have an advantage in real-time
 311 applications.

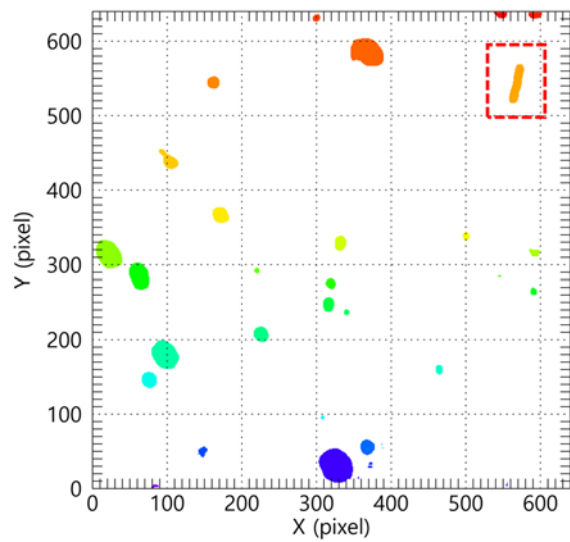
312 4.3 Estimation of DSD and rain rate

313 The rain streaks image presented in Fig. 8(c) was not considered for the final DSD estimation because of noise and factors
 314 other than rain caused by the sudden brightness change. As described in Section 3, a low-pass filter was first applied to the
 315 rain streaks image.

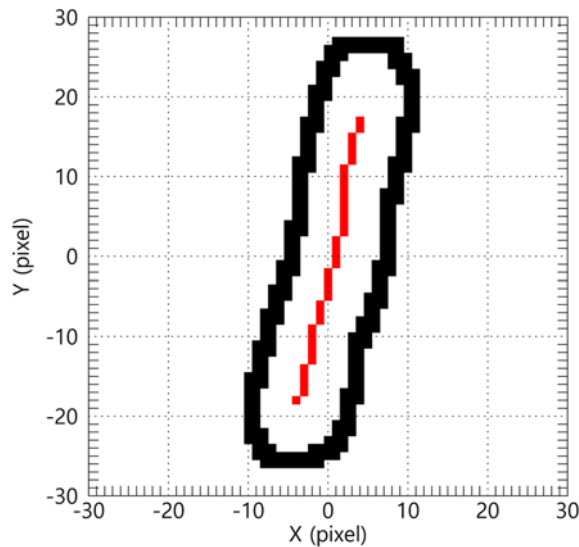
316 The 10×10 kernel was applied considering the total image size (640×640), and each grid value of the kernel was set to
 317 0.01. The set kernel was filtered by convolution pixel by pixel. Moreover, the convolution was performed once more using the
 318 following 2D kernel $\begin{bmatrix} 0 & 1 & 0 \\ -1 & 0 & 1 \\ 0 & -1 & 0 \end{bmatrix}$ to highlight the rim of the rain streaks. A background layer with a value of 0 and a
 319 part not in the image were separated to extract the rain streaks, which were labeled one by one to identify each rain streak from
 320 the image. Fig. 9(a) illustrates the example result after performing the processes described above in Fig. 8(c). Each rain streak
 321 was then separated and labeled, as in Fig. 9(b).



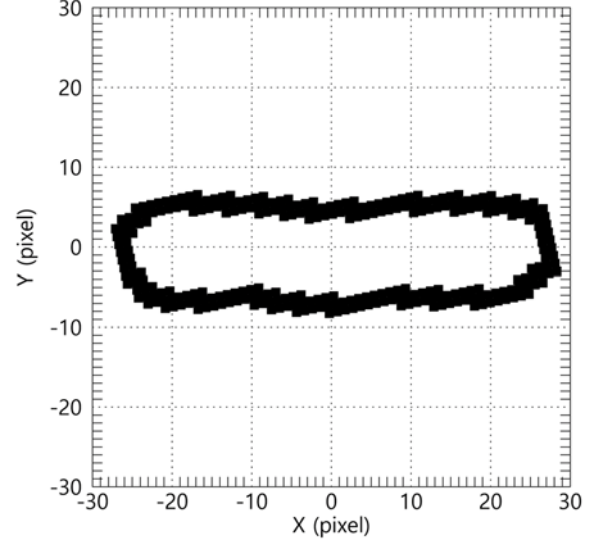
(a) Rain streaks image refined by low-pass filter



(b) Separated and labeled rain streaks



(c) Center axis for a rain streak



(d) Rotated rain streak considering the canting angle

322 **Figure 9. Extraction example of rain streak based on the proposed algorithm.**

323 The border information of each rain streak needed to be obtained. The center axis was calculated by connecting the center
 324 (median) of the minimum pixel and maximum pixel values of the x-axis for each y-axis using border information. The angle
 325 of rain streak was obtained from the slope value obtained by calculating the linear function through the center axis's x and y
 326 pixel number values. Fig. 9(c) is an example of the extraction of a rain streak extracted from the image of Fig. 9(b).

327 The drop angle was then calculated, and the rain streak was rotated using the angle information. Raindrops can be broken
 328 up by strong wind or collisions between raindrops during falling. The maximum difference value between the minimum and
 329 maximum pixel number values of the y-axis calculated using border information of the rotated rain streak was used to calculate
 330 the raindrop diameter and exclude the influence of the distorted shape of rain streak by break up (Fig. 9(d)) (Testik, 2009;

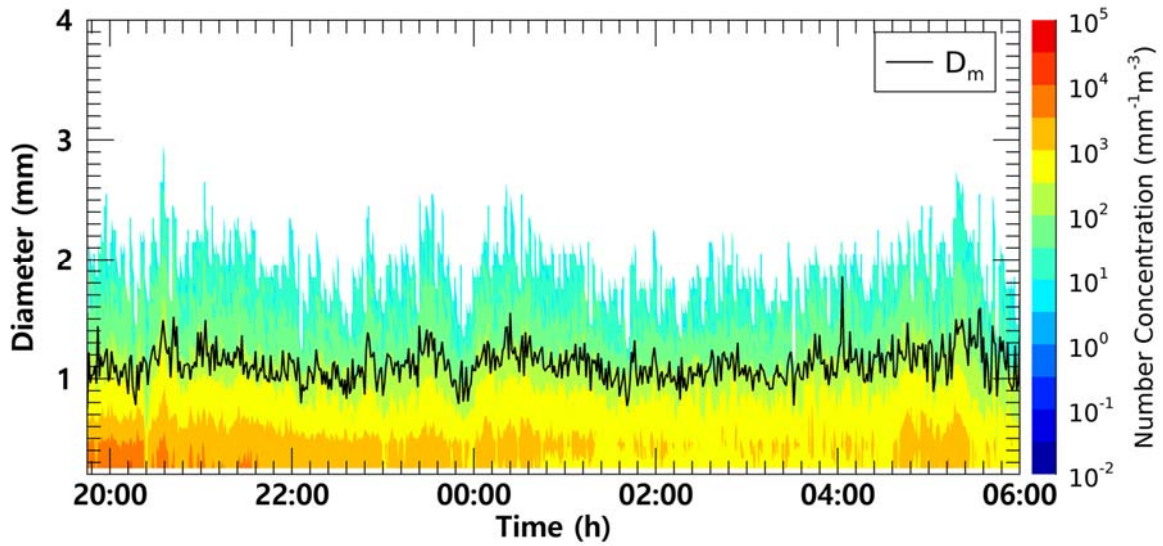
331 Testik and Pei, 2017). Fig. 9(d) illustrates the result of the final process. If the rain streaks overlap, the diameter of the raindrops
332 can be estimated as large. To reduce the overestimation of raindrop diameter, this study tried to find the main central axis
333 coordinates of overlapping rain streaks and set the longest central axis as the representative value. Then, estimate the primary
334 diameter by calculating the distance between each pixel value of the set central axis and the edge pixels of rain streaks.

335 Fig. 10 illustrates the time series of the number concentration and D_m obtained from CCTV and PARSIVEL. From 1945
336 LST to 2350 LST, the maximum number concentration of lower than $1,000 \text{ mm}^{-1}\text{m}^{-3}$ was observed from the PARSIVEL
337 observation, and from 2000 LST to 2010 LST, a number concentration lower than $100 \text{ mm}^{-1}\text{m}^{-3}$ was observed. At 2005 LST,
338 large raindrops (of 3.8 mm) were observed, resulting in a sharp increase in D_m above 2 mm. In contrast, in the results based on
339 CCTV images, the number concentration of less than $10,000 \text{ mm}^{-1}\text{m}^{-3}$ was continuously demonstrated during the entire analysis
340 period, and a number concentration greater than $5,000 \text{ mm}^{-1}\text{m}^{-3}$ was observed before 2200 LST. Because the proportion of
341 small drops was high, D_m was predominantly less than 1.5 mm.

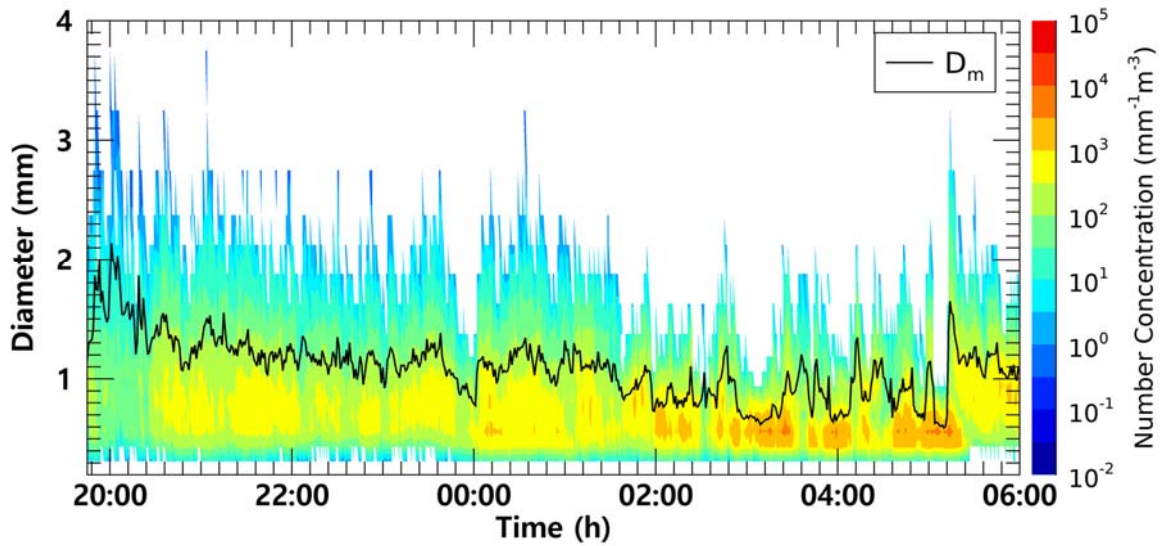
342 From 0000 LST to 0100 LST, both CCTV and PARSIVEL-based data had a predominant maximum diameter of about 2.4
343 mm. At 0035 LST, raindrops larger than 3.2 mm were observed in PARSIVEL, but raindrops less than 3 mm were not observed
344 in CCTV. However, the number concentration of small diameters of 0.5 mm or less had similar values between 1,000 and
345 $5,000 \text{ mm}^{-1}\text{m}^{-3}$. Despite the difference in the maximum size of the drops, there was no predominant difference in the D_m
346 because the number concentration of raindrops smaller than 1 mm had similar values.

347 From 0300 LST to 0530 LST, number concentrations higher than $5,000 \text{ mm}^{-1}\text{m}^{-3}$ in the raindrops smaller than 1 mm were
348 observed using PARSIVEL. However, CCTV data revealed that number concentrations less than $5,000 \text{ mm}^{-1}\text{m}^{-3}$ were
349 consistently observed. From 0500 LST to 0510 LST, CCTV image-based number concentration consistently appeared as about
350 1.2 mm, whereas D_m was smaller than 0.7 mm in PARSIVEL. The cause for the rapid decrease in D_m of the PARSIVEL was
351 that the CCTV-based maximum diameter is about 2.4 mm, which was similar to the PARSIVEL observation data, but the
352 number concentration of 0.5 to 0.6 mm raindrops observed by PARSIVEL had a large value of more than $10,000 \text{ mm}^{-1}\text{m}^{-3}$.

353
354



(a) CCTV



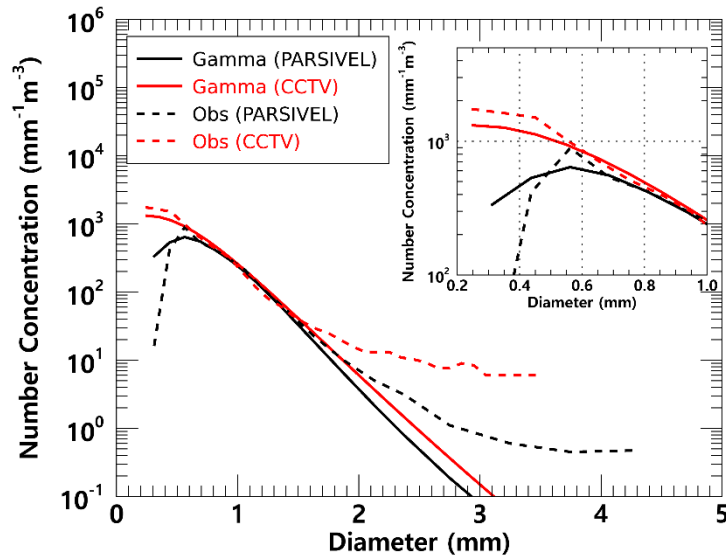
(b) PARSIVEL

355 Figure 10. Time series of number concentration and D_m (black coloured line) from (a) the surveillance camera images, (b) the
 356 PARSIVEL observation data from 2145 LST on March 25 to 0600 LST on March 26, 2022 (case 1).

357 Fig. 11 illustrates the average number concentration versus diameter of raindrops calculated using CCTV image and
 358 PARSIVEL observation data from 1945 LST on March 25 to 0600 LST on March 26, 2022. The PARSIVEL disdrometer data
 359 has a fixed raindrop diameter channel; thus, it can differ in number concentration depending on the diameter channel setting.

360 Therefore, in this study, the simulated DSD through the gamma model was also analyzed to compare the distribution of rainfall
361 particles.

362 For raindrop diameters from 0.7 to 1.5 mm, the simulated and observed number concentrations produced similar values.
363 However, above 1.5 mm, the model-based number concentration was under-simulated. From these results, in the precipitation
364 case selected in this study, the gamma model appears limited in simulating the number concentration of raindrops larger than
365 3 mm. In diameters from 0.2 to 1.0 mm and above 1.5 mm, the number concentration obtained from CCTV images tended to
366 be higher than that from PARSIVEL observation. PARSIVEL observation data decreased sharply for diameters smaller than
367 0.3 mm. In contrast, CCTV gradually increased the number concentration as the diameter decreased.

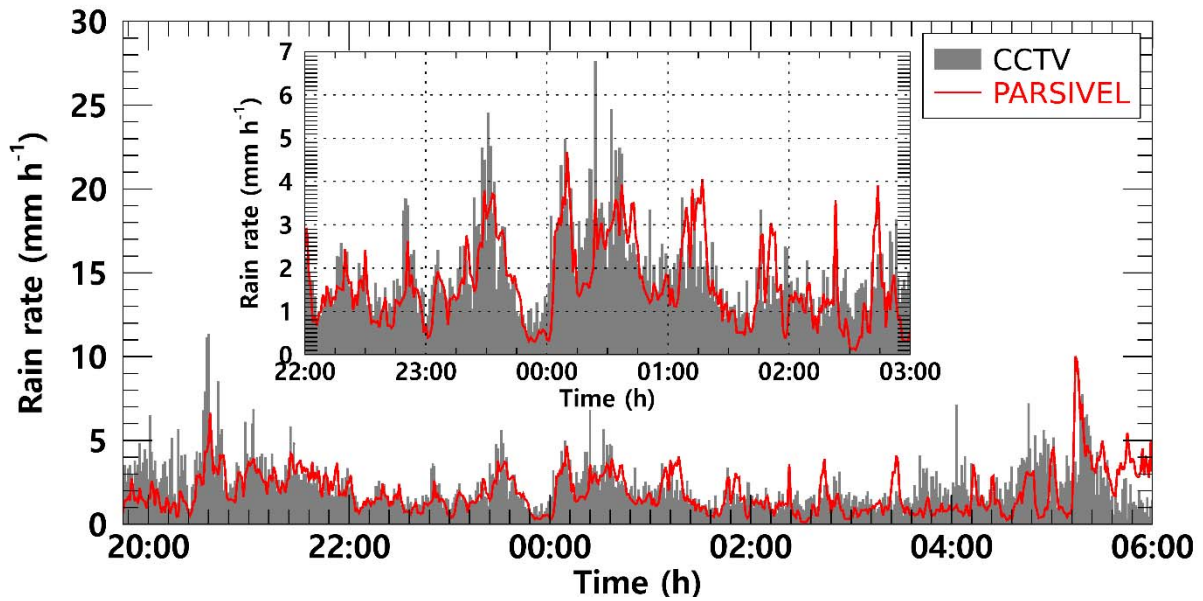


368 **Figure 11. Average number concentration versus diameter from the surveillance camera images and the PARSIVEL (case 1).**

369 Rainfall intensity was estimated based on the obtained number concentration from CCTV images and PARSIVEL. The
370 near (s_n) and far (s_f) focus planes were calculated as 718 and 1,648 mm from Eqs. (8) and (9). The DoF was calculated as 930
371 mm. The focal distance was set to 1 m, referring to previous studies (Dong et al., 2017; Jiang et al., 2019). The control volume
372 was 2.9 m^3 , applying Eq. (10) with the variables determined above. Fig. 12 illustrates the rain rate time series calculated using
373 CCTV images and PARSIVEL observation data. The increase or decrease in rain rate according to time change based on
374 CCTV data followed the trend of rainfall intensity change based on PARSIVEL observation data.

375 At 2037 LST, the PARSIVEL-based rain rate was 5.9 mm h^{-1} , but the CCTV-based rain rate was overestimated to be
376 higher than 10 mm h^{-1} . On the other hand, the CCTV-based rain rate was underestimated by about 2 mm h^{-1} than the
377 PARSIVEL-based rain rate at 0514 LST. Quantitative changes in CCTV-based rain rate showed a similar tendency to increase

378 and decrease the number concentration of raindrops smaller than 1 mm and the maximum diameter. From 0100 LST to 0200
 379 LST, when the number concentrations of CCTV and PARSIVEL had similar values, the rain rate also showed similar results.



380 **Figure 12.** The rain rate time series calculated from the surveillance camera images (gray bar) and PARSIVEL observation data
 381 (red line) from 2145 LST on March 25 to 0600 LST on March 26, 2022 (case 1).

382 Fig. 13 illustrates the scatter plot of the average rain rate every 15 min from the PARSIVEL observation and the CCTV
 383 images. Uncertainty exists in the resolution of the rain gauge in the 1 min step. Accordingly, the time step for analysis is set
 384 to 15 min. The slope of the regression line was 0.71 because the CCTV-based rain rate tended to be overestimated at a rain
 385 rate of weaker than 2 mm h⁻¹.

386 The cumulative average rainfall intensity every 15 min was weaker than 10 mm h⁻¹, concentrated at a rain rate less than 6
 387 mm h⁻¹, so the correlation coefficient (CC) was 0.64. Furthermore, the MAE, RMSE, and MAPE were 0.61 mm h⁻¹, 0.99 mm
 388 h⁻¹, and 48%. Differences according to rain rate can also be determined. The accuracy is higher at a rain rate smaller than 2
 389 mm h⁻¹ as a boundary. The MAE, RMSE, and MAPE were 0.29 mm h⁻¹, 0.72 mm h⁻¹, and 38% for a rain rate of 2 mm h⁻¹ or
 390 less, and 0.58 mm h⁻¹, 1.17 mm h⁻¹, and 55% for a rain rate above 2 mm h⁻¹.

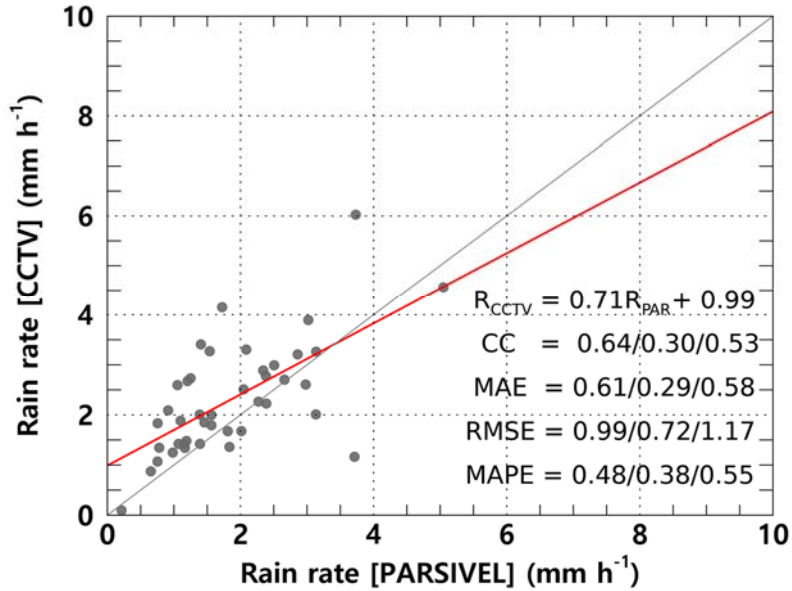
391 The statistical values of the rain rate and DSD parameters for the rainfall cases analyzed in this study are summarized in
 392 Table 3. The rain rate and D_m calculated using CCTV images were 0.459 mm h⁻¹ and 0.025 mm more than the values calculated
 393 using PARSIVEL observation data on average, respectively. A high rain rate and D_m were caused by overestimating the number
 394 concentration for raindrops larger than 1.5 mm confirmed in Fig. 10. The number concentration for the small diameter (less
 395 than 0.3 mm) was higher in the CCTV data than in the PARSIVEL data. Due to the high concentration value of the number
 396 concentration of raindrops below 0.5 mm and above 2 mm, the CCTV-based rain rate had a large value.

397 In the D_m calculated through the PARSIVEL observation data, the concentration change of small drops over time was large,
 398 and the variance (0.063 mm) of D_m was large due to the rapid change in number concentration. The variability of the maximum
 399 diameter was greater in the PARSIVEL observation data, but the variance of the rain rate was greater in the CCTV data. The
 400 large variability of the concentration of raindrops below 3 mm affected the change in the rain rate. Also, due to the high number
 401 concentration of small drops, the skewness of the CCTV (1.903) based rain rate had a higher value than that of the PARSIVEL
 402 (1.589) based rain rate. The low variability (0.063 mm) of the D_m calculated from CCTV data means that the change in the
 403 shape of the raindrop size distribution was small, supported by the low variance of Λ (3.016 mm^{-1}).

404 **Table 4. Statistical values of the rain rate and DSD parameters for case 1.**

		R (mm h^{-1})	D_m (mm)	$\log_{10}N_0$ ($\text{mm}^{-1}\mu\text{m}^{-3}$)	μ (unitless)	Λ (mm^{-1})
PARSIVEL	Mean	1.905	1.091	7.379	7.394	11.829
	Variance	1.667	0.063	15.170	35.975	88.288
	Skewness	1.589	0.551	2.470	2.015	2.714
	Kurtosis	5.189	1.233	7.751	5.132	9.165
CCTV	Mean	2.364	1.116	4.857	2.131	5.713
	Variance	1.998	0.021	0.472	1.680	3.016
	Skewness	1.903	0.536	1.109	0.628	1.151
	Kurtosis	6.073	1.041	2.188	0.739	2.506

405

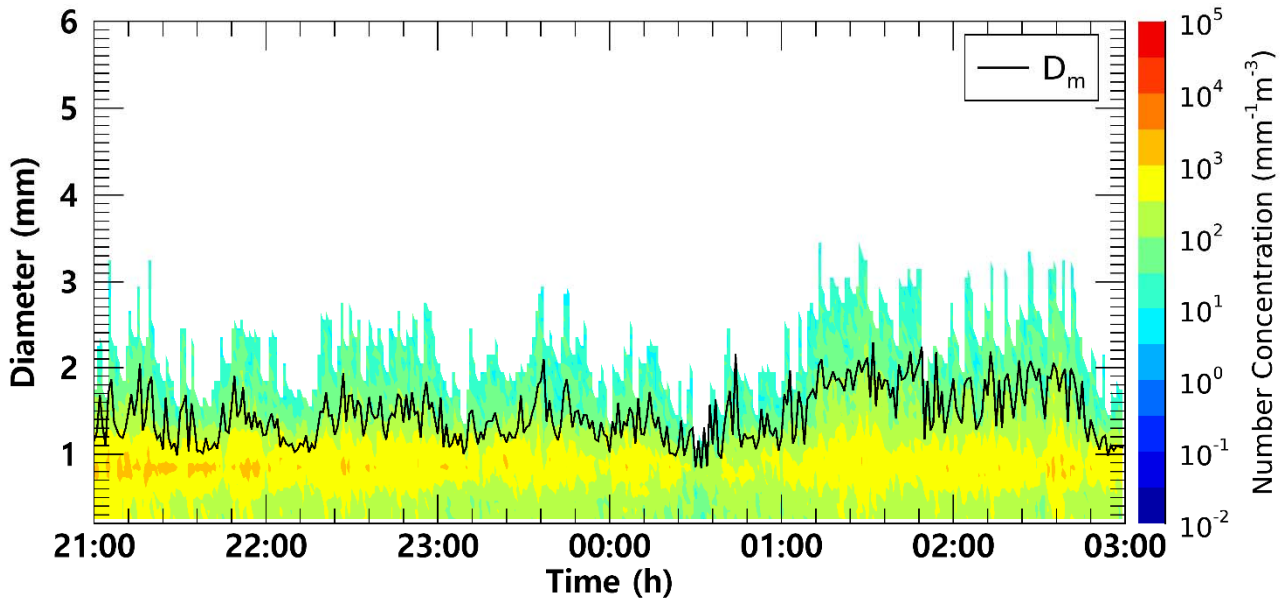


406 **Figure 13. Scatter plot of average rain rate every 15 minutes from the PARSIVEL observation and the surveillance camera images**
 407 **(case 1). Red line is linear regression. Scatter plot displays CC, MAE, RMSE, and MAPE for $R > 0 \text{ mm h}^{-1}$, $R < 2 \text{ mm h}^{-1}$, and $R \geq 2$**
 408 **mm h^{-1} (sequentially from left to right).**

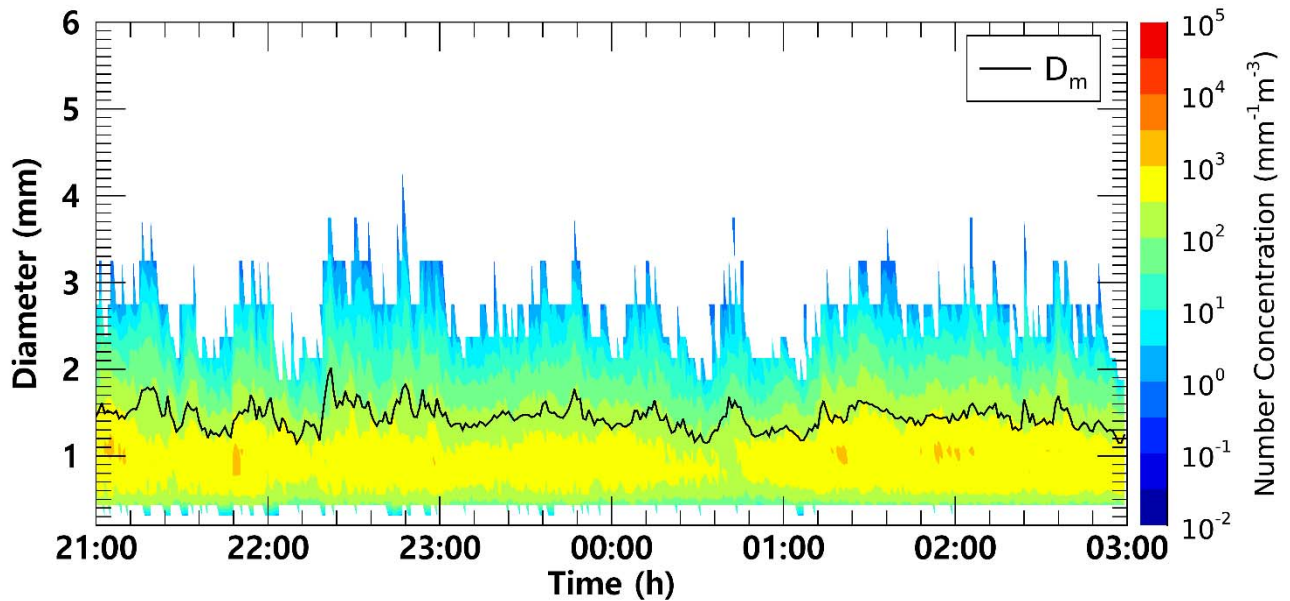
409 Fig. 14 illustrates the time series of the number concentration and D_m obtained from CCTV and PARSIVEL for case 2. In
410 both CCTV and PARSIVEL observation data, the number concentration for a diameter between 0.5 mm and 1.5 mm had a
411 value between $500 \text{ mm}^{-1}\text{m}^{-3}$ to $5,000 \text{ mm}^{-1}\text{m}^{-3}$, and there was no significant change in the number concentration with time.

412 The maximum diameter also consistently had a value close to about 3 mm, and the D_m was also similar to about 1.5 mm
413 because the maximum diameter and the number concentration of 1 mm intermediate drop had similar values.

414 From 0100 LST to 0230 LST, the maximum particle diameter through CCTV was overestimated, resulting in a large value
415 close to 3.5 mm. As a result, the D_m value increased significantly to more than 2 mm. PARSIVEL data showed a sharp decrease
416 in the number concentration of 1 mm drops at 0030 LST, and an increase in D_m under the influence of the decreased number
417 concentration. However, in the case of CCTV, only raindrops smaller than 1.5 mm were observed at the time, and there was a
418 similar decrease in D_m (about 1.1 mm).



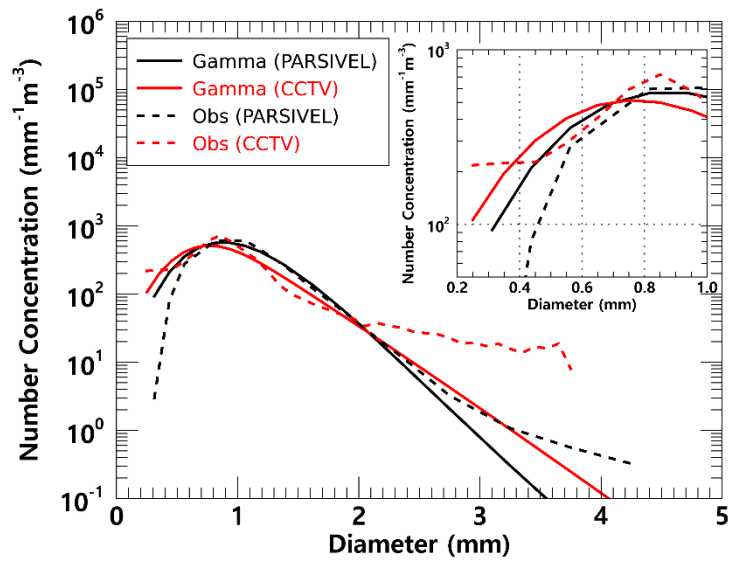
(a) CCTV



(b) PARSIVEL

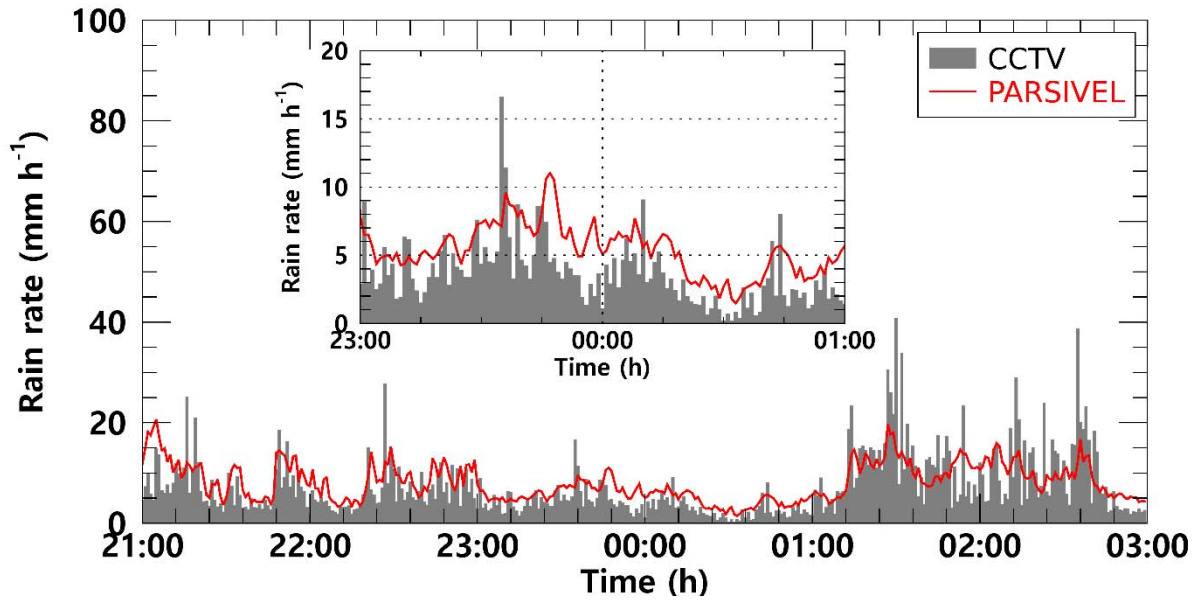
419 Figure 14. Time series of number concentration and D_m (black coloured line) from (a) the surveillance camera images, (b) the
 420 PARSIVEL observation data from 2100 LST on September 5 to 0300 LST on September 6, 2022 (case 2).

421 As clearly shown in Fig. 14, there was no significant difference in number concentration according to the time change. The
 422 average number concentration distribution also showed similar results because the number concentration values were
 423 concentrated at $1,000 \text{ mm}^{-1}\text{m}^{-3}$ concentration in both observation instruments. (Fig. 15). As in case 1, PARSIVEL observation
 424 data showed a tendency to underestimate in sections less than 0.5 mm and underestimated in sections larger than 2 mm
 425 compared to CCTV data. The diameter section where CCTV data is underestimated compared to PARSIVEL data was from 1
 426 mm to 2 mm. Since the number concentration of the CCTV data was underestimated in this section, the rain rate based on the
 427 number concentration data was also underestimated compared to the rainfall intensity based on the PARSIVEL data.



428 **Figure 15. Average number concentration versus diameter from the surveillance camera images and the PARSIVEL (case 2).**

429 Between 2100 LST on September 5 and 0100 LST on September 6, when the number concentration of about 1 mm
 430 raindrops is similar and the maximum diameter size is similar, the rain rate time series distribution has a value of about 5 mm
 431 h⁻¹ and has a very similar flow. However, between 0130 LST and 0300 LST, which is a period with an overestimation of
 432 raindrop diameter in CCTV observation data, the increase and decrease in rain rate were similar. However, the magnitude of
 433 the increase and decrease in rain rate differed every 15 minutes. During that time, the maximum rain rate was less than 20 mm
 434 h⁻¹ in the PARSIVEL observation data, while strong rainfall of 30 mm h⁻¹ or more was observed in the CCTV observation data.

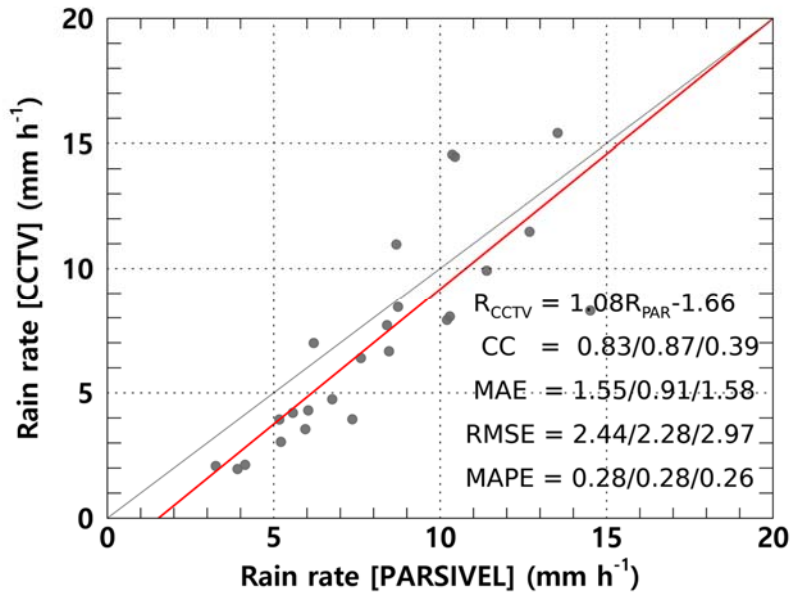


435 Figure 16. The rain rate time series calculated from the surveillance camera images (gray bar) and PARSIVEL observation data
 436 (red line) from 2100 LST on September 5 to 0300 LST on September 6, 2022 (case 2).

437 Fig. 17 illustrates the scatter plot of the average rain rate every 15 min from the PARSIVEL observation and the CCTV
 438 images for case 2. Compared to case 1, case 2 was a strong rainfall case with a rain rate of about 8.94 mm h⁻¹. Compared to
 439 the PARSIVEL observation data, the CCTV observation data showed a larger D_m by 0.221 mm, while the $\log_{10}N_0$ showed a
 440 small feature of 1.1 mm⁻¹μm⁻³. As the weight of medium and large drops over 1 mm increased, μ and Λ showed lower values
 441 of 4.262 and 5.397 mm⁻¹, respectively (Table 5). According to the 15-minute cumulative rain rate comparison result, the rain
 442 rate based on CCTV image data tends to be underestimated when it is less than 10 mm h⁻¹. Conversely, there was a tendency
 443 to overestimate the rainfall period of 10 mm h⁻¹ or more. This tendency was confirmed in case 1 which may be caused by
 444 recognizing overlapping rain streaks as a single big raindrop. MAPE had a low value of 0.3% or less regardless of the rain rate,
 445 and even though the rainfall intensity was relatively large compared to case 1, MAE and RMSE did not significantly increase.
 446 This is because there was no abnormally large value of CCTV rainfall during the rainfall period of case 2 compared to case 1.

447 Table 5. Statistical values of the rain rate and DSD parameters for case 2.

		R (mm h ⁻¹)	D_m (mm)	$\log_{10}N_0$ (mm ⁻¹ μm ⁻³)	μ (unitless)	Λ (mm ⁻¹)
PARSIVEL	Mean	8.12	1.445	5.900	6.379	7.341
	Variance	13.82	0.020	1.160	6.498	5.596
	Skewness	0.65	0.447	1.061	0.9467	1.198
	Kurtosis	-0.13	0.472	2.480	1.818	2.792
CCTV	Mean	8.94	1.666	4.813	4.262	5.397
	Variance	69.33	0.121	1.185	4.577	6.714
	Skewness	2.75	0.355	2.596	1.903	2.640
	Kurtosis	11.71	-0.202	8.962	5.714	9.756



449 Fig. 17. Scatter plot of average rain rate every 15 minutes from the PARSIVEL observation and the surveillance camera images
 450 (case 2). Red line is linear regression. Scatter plot displays CC, MAE, RMSE, and MAPE for $R > 0 \text{ mm h}^{-1}$, $R < 5 \text{ mm h}^{-1}$, and $R \geq 5$
 451 mm h^{-1} (sequentially from left to right).

452 6 Conclusion

453 This study estimated DSD with an infrared surveillance camera, based on which rainfall intensity was also estimated. Rain
 454 streaks were extracted using a KNN-based algorithm. The rainfall intensity was estimated based on DSD using physical optics
 455 analysis. A rainfall event was selected, and the applicability of the method in this study was examined. The estimated DSD
 456 was verified using a PARSIVEL. The results from this study can be summarized as follows.

457 KNN-based algorithm illustrates suitable performance in separating the rain streaks and background layers. Furthermore,
 458 the possibility of separation for each rain streak and estimation of DSD was sufficient.

459 The number concentration of raindrops obtained through the CCTV images was similar to the actual PARSIVEL observed
 460 number concentration in the 0.5 to 1.5 mm section. In the small raindrops in the section of 0.4 mm or less, the PARSIVEL
 461 observation data underestimates the actual DSD. However, the CCTV image-based rain rate had an advantage over the
 462 raindrop-based data—the number concentration decreased rapidly as the number concentration gradually increased in the 0.2–
 463 0.3 mm diameter section.

464 The maximum raindrop diameter and number concentration of less than 1 mm produced similar results during the period
 465 with a high ratio of diameters less than 3 mm. However, the number concentration was overestimated during the period when

466 raindrops larger than 3 mm were observed. The CCTV image-based data revealed that the rain rate was overestimated because
 467 of the overestimation of raindrops larger than 3 mm. After comparing with the 15-min cumulative PARSIVEL rain rate, the
 468 CCs—MAE, RMSE, and MAPE of case 1 (case 2)—were 0.61 mm h⁻¹ (1.55 mm h⁻¹), 0.99 mm h⁻¹ (1.43 mm h⁻¹), and 48%
 469 (44%). The differences according to rain rate can be identified. The accuracy is higher at a rain rate smaller than 10 mm h⁻¹ as
 470 a boundary.

471 The rain rate and D_m calculated using CCTV images exhibited similar average values. The overestimated number
 472 concentration of 1.5 mm or larger caused high kurtosis for the rain rate and D_m of CCTV-based data and a low μ value. Because
 473 of the high number concentration for raindrops larger than 3 mm of CCTV, the PARSIVEL observation data had a higher A
 474 value than the result based on the CCTV data.

475 In this study, DSD was estimated using an infrared surveillance camera; the rain rate was also estimated. Consequently,
 476 we could confirm the possibility of estimating an image-based DSD and rain rate obtained based on low-cost equipment in
 477 dark conditions. Though the infrared surveillance camera considered in this study will not be able to replace traditional
 478 observation devices, if future studies can be continued to secure robustness, it will be an excellent complement to the existing
 479 observation system in terms of spatiotemporal resolution and accuracy improvement.

480 **Appendix. The diameter and fall velocity information for each diameter channel class.**

481 **Table 1. The representative diameter and spread for each diameter channel class.**

Class number	Class average (mm)	Class spread (mm)	Class number	Class average (mm)	Class spread in (mm)
1	0.062	0.125	17	3.250	0.500
2	0.187	0.125	18	3.750	0.500
3	0.312	0.125	19	4.250	0.500
4	0.437	0.125	20	4.750	0.500
5	0.562	0.125	21	5.500	1.000
6	0.687	0.125	22	6.500	1.000
7	0.812	0.125	23	7.500	1.000
8	0.937	0.125	24	8.500	1.000
9	1.062	0.125	25	9.500	1.000
10	1.187	0.125	26	11.000	2.000
11	1.375	0.250	27	13.000	2.000
12	1.625	0.250	28	15.000	2.000
13	1.875	0.250	29	17.000	2.000
14	2.125	0.250	30	19.000	2.000
15	2.375	0.250	31	21.500	3.000
16	2.750	0.500	32	24.500	3.000

482 **Table 2. The representative fall velocity and spread for each diameter channel class.**

Class number	Class average (m s ⁻¹)	Class spread (m s ⁻¹)	Class number	Class average (m s ⁻¹)	Class spread (m s ⁻¹)
1	0.050	0.100	17	2.600	0.400
2	0.150	0.100	18	3.000	0.400
3	0.250	0.100	19	3.400	0.400
4	0.350	0.100	20	3.800	0.400
5	0.450	0.100	21	4.400	0.800
6	0.550	0.100	22	5.200	0.800
7	0.650	0.100	23	6.000	0.800
8	0.750	0.100	24	6.800	0.800
9	0.850	0.100	25	7.600	0.800
10	0.950	0.100	26	8.800	1.600
11	1.100	0.200	27	10.400	1.600
12	1.300	0.200	28	12.000	1.600
13	1.500	0.200	29	13.600	1.600
14	1.700	0.200	30	15.200	1.600
15	1.900	0.200	31	17.600	3.200
16	2.200	0.400	32	20.800	3.200

483 **Data availability**

484 The raw videos and data used in the analysis can be downloaded from <https://doi.org/10.6084/m9.figshare.c.6392430.v1>, and
485 the sample codes are available in a public GitHub repository from https://github.com/jinwook213/Rain_CCTV.git.

486 **Acknowledgements**

487 This research was supported by the Korea Meteorological Administration Research and Development Program (KMI2022-
488 01910), by Basic Science Research Program through the National Research Foundation of Korea (NRF) funded by the Ministry
489 of Education (2022R1I1A1A01065554 and 2022R1A6A3A01087041), and by the Chung-Ang University Graduate Research
490 Scholarship in 2021.

491 **References**

- 492 Allamano, P., Croci, A., and Laio, F.: Toward the camera rain gauge. *Water Resour. Res.* 51 (3), 1744-1757, 2015
493 Atlas, D., Srivastava, R. C., and Sekhon, R. S.: Doppler radar characteristics of precipitation at vertical incidence. *Rev.*
494 *Geophys.* 11 (1), 1–35, 1973.
495 Avanzato, R. and Beritelli, F.: A cnn-based differential image processing approach for rainfall classification. *Adv. Sci. Technol.*
496 *Eng. Syst. J.* 5 (4), 438-444, 2020.

497 Bouwmans, T., El Baf, F., and Vachon, B.: Statistical background modeling for foreground detection: A survey. In: Chen, C.
498 H. (Ed.) Handbook of pattern recognition and computer vision, fourth ed. World Scientific, Singapore, pp. 181-199, 2010

499 Cai, F., Lu, W., Shi, W., and He, S.: A mobile device-based imaging spectrometer for environmental monitoring by attaching
500 a lightweight small module to a commercial digital camera. *Sci. Rep.* 7 (1), 1-9, 2017.

501 Colli, M., Lanza, L. G., La Barbera, P., and Chan, P. W.: Measurement accuracy of weighing and tipping-bucket rainfall
502 intensity gauges under dynamic laboratory testing. *Atmos. Res.*, 144, 186-194, 2014.

503 Deng, L. J., Huang, T. Z., Zhao, X. L., and Jiang, T. X.: A directional global sparse model for single image rain removal. *Appl.*
504 *Math. Model.* 59, 662-679, 2018.

505 Dong, R., Liao, J., Li, B., Zhou, H., and Crookes, D.: Measurements of rainfall rates from videos. In 2017 10th International
506 Congress on Image and Signal Processing, BioMedical Engineering and Informatics, IEEE, Shanghai, China, 14-16 October,
507 pp. 1-9, 2017.

508 Duthon, P., Bernardin, F., Chausse, F., and Colomb, M.: Benchmark for the robustness of image features in rainy conditions.
509 *Mach. Vis. Appl.* 29 (5), 915-927, 2018.

510 Famiglietti, J. S., Cazenave, A., Eicker, A., Reager, J. T., Rodell, M., and Velicogna, I.: Satellites provide the big picture. *Sci.*
511 349 (6249), 684-685, 2015.

512 Friedrich, K., Kalina, E. A., Masters, F. J., and Lopez, C. R.: Drop-size distributions in thunderstorms measured by optical
513 disdrometers during VORTEX2. *Mon. Weather Rev.* 141 (4), 1182-1203, 2013.

514 Garg, K. and Nayar, S. K.: Vision and rain. *Int. J. Comput. Vis.* 75 (1), 3-27, 2007.

515 Guo, B., Han, Q., Chen, H., Shangguan, L., Zhou, Z., and Yu, Z.: The emergence of visual crowdsensing: Challenges and
516 opportunities. *IEEE Commun. Surv. Tutor.* 19 (4), 2526-2543, 2017.

517 Guo, H., Huang, H., Sun, Y. E., Zhang, Y., Chen, S., and Huang, L.: Chaac: Real-time and fine-grained rain detection and
518 measurement using smartphones. *IEEE Internet Things J.* 6 (1), 997-1009, 2019

519 Haberlandt, U. and Sester, M.: Areal rainfall estimation using moving cars as rain gauges-A modelling study. *Hydrol. Earth*
520 *Syst. Sci.* 14 (7), 1139-1151, 2010.

521 Hua, X. S.: The city brain: Towards real-time search for the real-world. In The 41st International ACM SIGIR Conference on
522 Research & Development in Information Retrieval, New York, NY, 8-12 July. pp. 1343-1344, 2018

523 Jiang, S., Babovic, V., Zheng, Y., and Xiong, J.: Advancing opportunistic sensing in hydrology: A novel approach to measuring
524 rainfall with ordinary surveillance cameras. *Water Resour. Res.* 55 (4), 3004-3027, 2019.

525 Jiang, T. X., Huang, T. Z., Zhao, X. L., Deng, L. J., and Wang, Y.: Fastderain: A novel video rain streak removal method using
526 directional gradient priors. *IEEE Trans. Image Process.* 28 (4), 2089-2102, 2018.

527 Kathiravelu, G., Lucke, T., and Nichols, P.: Rain drop measurement techniques: A review. *Water*, 8 (1), 29, 2016.

528 Keating, M. P.: Geometric, physical, and visual optics, Second ed. Butterworth-Heinemann, Oxford, UK, 2002.

529 Kidd, C., Becker, A., Huffman, G. J., Muller, C. L., Joe, P., Skofronick-Jackson, G., and Kirschbaum, D. B.: So, how much
530 of the Earth's surface is covered by rain gauges?. *Bull. Am. Meteorol. Soc.* 98 (1), 69-78, 2017.

531 Kim, J. H., Sim, J. Y., and Kim, C. S.: Video deraining and desnowing using temporal correlation and low-rank matrix
532 completion. *IEEE Trans. Image Process.*, 24 (9), 2658-2670, 2015.

533 Li, Y., Tan, R. T., Guo, X., Lu, J., and Brown, M. S.: Rain streak removal using layer priors. In 2016 IEEE Conference on
534 Computer Vision and Pattern Recognition, IEEE, Las Vegas, NV, 27-30 June, pp. 2736-2744, 2016.

535 Löffler-Mang, M. and Joss, J.: An optical disdrometer for measuring size and velocity of hydrometeors. *J. Atmos. Ocean.
536 Technol.* 17 (2), 130–139, 2000.

537 Marshall, J. S. and Palmer, W. M.: The distribution of raindrops with size. *J. Meteor.* 5, 165–166, 1948.

538 McCabe, M. F., Rodell, M., Alsdorf, D. E., Miralles, D. G., Uijlenhoet, R., Wagner, W., Lucieer, A., Houborg, R., Verhoest,
539 N. E. C., Franz, T. E., Shi, J., Gao, H., and Wood, E. F.: The future of earth observation in hydrology. *Hydrol. Earth Syst. Sci.*
540 21 (7), 3879-3914, 2017.

541 Michaelides, S., Levizzani, V., Anagnostou, E., Bauer, P., Kasparis, T., and Lane, J. E.: Precipitation: Measurement, remote
542 sensing, climatology and modeling. *Atmos. Res.* 94 (4), 512-533, 2009.

543 Nemeth, K. and Hahn, J. M.: Enhanced precipitation identifier and new generation of present weather sensor by OTT
544 Messtechnik, In WMO/CIMO Technical Conference, Germany, 2005.

545 Nottle, A., Harborne, D., Braines, D., Alzantot, M., Quintana-Amate, S., Tomsett, R., Kaplan, L., Srivastava, M. B.,
546 Chakraborty, S., and Preece, A.: Distributed opportunistic sensing and fusion for traffic congestion detection. In 2017 IEEE
547 SmartWorld, Ubiquitous Intelligence & Computing, Advanced & Trusted Computed, Scalable Computing & Communications,
548 Cloud & Big Data Computing, Internet of People and Smart City Innovation, IEEE, San Francisco, CA, 4-8 August, pp. 1-6,
549 2017.

550 Qasim, S., Khan, K. N., Yu, M., and Khan, M. S.: Performance evaluation of background subtraction techniques for video
551 frames. In 2021 International Conference on Artificial Intelligence, IEEE, Islamabad, Pakistan, 5-7 April, pp. 102-107, 2021.

552 Overeem, A., Leijnse, H., and Uijlenhoet, R.: Two and a half years of country-wide rainfall maps using radio links from
553 commercial cellular telecommunication networks. *Water Resour. Res.* 52 (10), 8039-8065, 2016.

554 Rabiei, E., Haberlandt, U., Sester, M., and Fitzner, D.: Rainfall estimation using moving cars as rain gauges—laboratory
555 experiments. *Hydrol. Earth Syst. Sci.* 17 (11), 4701-4712, 2013.

556 Rabiei, E., Haberlandt, U., Sester, M., Fitzner, D., and Wallner, M.: Areal rainfall estimation using moving cars—computer
557 experiments including hydrological modeling. *Hydrol. Earth Syst. Sci.* 20 (9), 3907-3922, 2016.

558 Santhaseelan, V. and Asari, V. K.: Utilizing local phase information to remove rain from video. *Int. J. Comput. Vis.*, 112 (1),
559 71-89, 2015.

560 Schmidt, J. M., Flatau, P. J., Harasti, P. R., Yates, R. D., Littleton, R., Pritchard, M. S., Fischer, J. M., Fischer, E. J., Kohri,
561 W. J., Vetter, J. R., Richman, S., Baranowski, D. B., Anderson, M. J., Fletcher, E., and Lando, D. W.: Radar observations of
562 individual rain drops in the free atmosphere. *Proc. Natl. Acad. Sci.* 109 (24), 9293-9298, 2012.

563 Smith, P. L.: Raindrop size distributions: Exponential or gamma—Does the difference matter?. *J. Appl. Meteorol. Climatol.*,
564 42 (7), 1031-1034, 2003.

565 Testik, F. Y.: Outcome regimes of binary raindrop collisions. *Atmos. Res.* 94 (3), 389–399, 2009.

566 Testik, F. Y. and Pei, B.: Wind effects on the shape of raindrop size distribution. *J. Hydrometeorol.* 18 (5), 1285-1303, 2017.

567 Tokay, A. and Short, D. A.: Evidence from tropical raindrop spectra of the origin of rain from stratiform versus convective
568 clouds. *J. Appl. Meteorol. Climatol.* 35 (3), 355–371, 1996.

569 Tripathi, A. K. and Mukhopadhyay, S.: Removal of rain from videos: A review. *Signal Image Video Process.* 8 (8), 1421-
570 1430, 2014.

571 Trnovszký, T., Sýkora, P., and Hudec, R.: Comparison of background subtraction methods on near infra-red spectrum video
572 sequences. *Procedia Eng.*, 192, 887-892, 2017.

573 Ulbrich, C. W.: Natural variations in the analytical form of the raindrop size distribution. *J. Appl. Meteorol. Climatol.* 22 (10),
574 1764–1775, 1983.

575 Vivekanandan, J., Zhang, G., and Brandes, E.: Polarimetric radar estimators based on a constrained gamma drop size
576 distribution model. *J. Appl. Meteorol.* 43 (2), 217-230, 2004.

577 Wang, X., Wang, M., Liu, X., Glade, T., Chen, M., Xie, Y., Yuan, Hao., and Chen, Y.: Rainfall observation using surveillance
578 audio. *Appl. Acoust.* 186, 108478, 2022.

579 Yang, P. and Ng, T. L.: Gauging through the crowd: A crowd-sourcing approach to urban rainfall measurement and storm
580 water modeling implications. *Water Resour. Res.* 53 (11), 9462-9478, 2017.

581 Yuter, S. E. and Houze Jr, R. A.: Measurements of raindrop size distributions over the Pacific warm pool and implications for
582 Z–R relations. *J. Appl. Meteorol.* 36 (7), 847-867, 1997.

583 Zen, R., Arsa, D. M. S., Zhang, R., Er, N. A. S., and Bressan, S.: Rainfall estimation from traffic cameras. In: Hartmann, S.,
584 Küng, J., Chakravarthy, S., Anderst-Kotsis, G., Tjoa, A., Khalil, I. (Eds.) *Database and Expert Systems Applications*, Springer,
585 Cham, Switzerland, pp. 18-32, 2019.

586 Zivkovic, Z. and Van Der Heijden, F.: Efficient adaptive density estimation per image pixel for the task of background
587 subtraction. *Pattern Recognit. Lett.* 27 (7), 773-780, 2006.